Yip, S. T. H., Biggs, J. J., Edmonds, M., & Liggins, P. (2024). The role of pre-eruptive gas segregation on co-eruptive deformation and SO2 emissions. *Earth and Planetary Science Letters*, *626*(2024), [118548]. https://doi.org/doi.org/10.1016/j.epsl.2023.118548

Publisher's PDF, also known as Version of record

License (if available):
CC BY

Link to published version (if available):
doi.org/10.1016/j.epsl.2023.118548

Link to publication record in Explore Bristol Research
PDF-document

University of Bristol - Explore Bristol Research

General rights

This document is made available in accordance with publisher policies. Please cite only the published version using the reference above. Full terms of use are available:
http://www.bristol.ac.uk/red/research-policy/pure/user-guides/ebr-terms/

Earth Planet. Sci. Lett. 626 (2024) 118548

Contents lists available at ScienceDirect

Earth and Planetary Science Letters

journal homepage: www.elsevier.com/locate/epsl

The role of pre-eruptive gas segregation on co-eruptive deformation and SO_2 emissions

Stanley Tze Hou Yip [a,b,*], Juliet Biggs [a,b], Marie Edmonds [a,c], Philippa Liggins [d]

[a] Centre for the Observation and Modelling of Earthquakes, Volcanoes and Tectonics (COMET), United Kingdom
[b] School of Earth Sciences, University of Bristol, Wills Memorial Building, Bristol, BS8 1RJ, United Kingdom
[c] Department of Earth Sciences, University of Cambridge, Cambridge, CB2 3EQ, United Kingdom
[d] Oxford Research Software Engineering, University of Oxford, Oxford, OX1 3NP, United Kingdom

ARTICLE INFO

Editor: C.M. Petrone

Keywords:
volcano deformation
SO_2 degassing
magma compressibility
exsolved volatile segregation

ABSTRACT

The presence of exsolved gas bubbles influences measurements of both volcanic surface deformation and SO_2 emissions. In a closed-system, exsolved volatiles remain within the melt but in an open-system, the decoupled gas phase can either outgas or accumulate, leading to large variations magmatic gas fraction. Here we investigate the role of gas volume fraction and gas segregation processes on magma properties and co-eruptive monitoring data. First we use thermodynamic models of gas exsolution to model gas volume fraction and magma compressibility, and use these to calculate SO_2 emissions and co-eruptive volume change. We find that volume change is equally sensitive to magma compressibility and chamber compressibility over realistic parameters ranges, and both must be considered when interpreting surface deformation data. Reservoir depth and magma composition are the dominant controls on gas volume fraction, but the initial content of H_2O and S have strong influences on volume change and SO_2 emissions, respectively. Pre-eruptive gas accumulation produces increased SO_2 emissions and muted co-eruptive deformation, while degassing has the opposite effect. We then compare our models to a compilation of data from 20 recent eruptions where measurements of volume change, SO_2 emissions and erupted volume are available. To the first order, shallow reservoirs produce smaller volume changes per volume erupted and silica-poor magmas yield greater co-eruptive volume changes than silica-rich systems, consistent with closed system degassing. Co-eruptive degassing causes high SO_2 emissions during effusive eruptions. Comparison between model predictions and observations suggests that all magmatic systems experience a certain degree of outgassing prior to an eruption. Our findings are consistent with current conceptual models of transcrustal magmatic systems consisting of heterogeneous mixtures of gas and melt and have important implications for the interpretation of surface deformation and SO_2 emission signals at all stages of the eruption cycle.

1. Introduction

Measurements of surface deformation and SO_2 emissions are becoming increasingly routine and can be used to study volcanic and magmatic processes and in the forecasting of eruptions (Biggs and Wright, 2020; Pritchard et al., 2022). However, most studies consider either deformation or SO_2 emissions in isolation (e.g., Sigmarsson et al., 2013; Hreinsdóttir et al., 2014; Hotta et al., 2019) or combine them in a qualitative manner (e.g., Sheldrake et al., 2017; Reath et al., 2020; Joseph et al., 2022). We seek to develop a robust physics-based framework that can combine measurements of deformation and SO_2 degassing to provide new insights into magmatic processes. The key to this framework is the exsolved volatile content of the magma which determines magma compressibility, and hence modulates observations of both surface deformation and SO_2 emissions (e.g., Kilbride et al., 2016; Yip et al., 2022).

Volatiles typically make up a few weight percent of magmas, yet are of significant importance in controlling the magnitude and style of volcanic eruptions (e.g., Woods and Huppert, 2003; Cashman, 2004; Cassidy et al., 2018). Volatile solubility is controlled by pressure, temperature and melt composition, and volatile exsolution can be driven by either magma ascent or isobaric crystallisation (e.g., Candela, 1997; Burgisser et al., 2015; Liggins et al., 2020). Once exsolved, the gas bubbles can decouple from the melt and whether they accumulate (e.g.,

* Corresponding author at: School of Earth Sciences, University of Bristol, Wills Memorial Building, Bristol, BS8 1RJ, United Kingdom.
E-mail address: stanley.th.yip@bristol.ac.uk (S.T.H. Yip).

https://doi.org/10.1016/j.epsl.2023.118548
Received 8 August 2023; Received in revised form 23 October 2023; Accepted 14 December 2023
Available online 20 December 2023
0012-821X/© 2023 The Author(s). Published by Elsevier B.V. This is an open access article under the CC BY license (http://creativecommons.org/licenses/by/4.0/).

Oppenheimer et al., 2015; Parmigiani et al., 2016), or escape via permeable networks (e.g., Chiodini et al., 2005; Kushnir et al., 2017; Colombier et al., 2021) has significant implications for the magnitude of co-eruptive deformation and degassing. We hypothesise that the accumulation of exsolved volatiles will 1) produce 'excess' SO_2 emissions during eruptions (e.g., Wallace and Gerlach, 1994; Wallace, 2001) and 2) reduce syn-eruptive surface deformation by increasing magma compressibility (Rivalta and Segall, 2008; Kilbride et al., 2016; Yip et al., 2022). Conversely, inter-eruptive degassing will reduce syn-eruptive SO_2 emissions and reduce magma compressibility such that the volume of material erupted is roughly equal to the subsurface volume change.

In this study, we use thermodynamic models to investigate the effects of exsolved gases on magma properties, deformation and SO_2 emissions. In Section 2, we explore the effects of varying magma composition and initial volatile contents and in Section 3, we explore the role of pre-eruptive volatile segregation processes (i.e., exsolved volatile accumulation at the reservoir roof, or the formation of a 'degassed plug'). Finally, in Section 4, we compare observations of real-world eruption data to our model predictions and discuss the implications of pre-eruptive exsolved volatile segregation on observations of volcanic deformation and SO_2 emissions.

2. Model setup

2.1. Thermodynamic framework

Volatile solubility is controlled by melt chemistry, pressure and temperature conditions and fugacity. Magmas can reach volatile saturation by either decompression during ascent or isobaric crystallisation during cooling (e.g., Candela, 1997; Edmonds and Woods, 2018). Thermodynamic models (e.g., MELTS (Ghiorso and Sack, 1995; Asimow, 1998); SolEx (Witham et al., 2012); D-Compress (Burgisser et al., 2015)) use solubility laws and petrological data to predict the proportion of each species (e.g., H_2O, CO_2, S) that will exsolve at given pressure, temperature, melt composition and f_{O_2} and hence the gas fraction of each species. However, these models do not include sulfide and sulfate capacity laws to model sulfur behaviour (Ding et al., 2023).

Here we use the Python-based model, EVo (Liggins et al., 2020, 2022), to model the exsolution of H_2O, CO_2 and SO_2 species in a C-O-H-S-Fe system during magma decompression. EVo uses the recently released thermodynamic models including the CO_2 solubility model of Eguchi and Dasgupta (2018), the sulfide capacity law from O'Neill (2021) and the sulfate capacity law from Nash et al. (2019) which is applicable at pressures of 300 MPa or less. We note that the sulfide capacity law used is most suitable for more reduced melts than those considered in our study (O'Neill, 2021). However, a recent study by Ding et al. (2023), which compared the different sulfide and sulfate capacity laws of Nash et al. (2019) and O'Neill and Mavrogenes (2022), shows that for a given temperature and composition the sulfur degassing pathways are similar regardless of the different laws used.

The thermodynamic model requires an estimate of initial volatile contents to begin calculations, which can be obtained using melt inclusions for basaltic magmas (Yip et al., 2022). However, for evolved magmas, where gas exsolution starts deep and a gas phase co-exists with the liquid magma during entrapment, melt inclusions often underestimate actual volatile content (Johnson et al., 1994; Scaillet and Pichavant, 2003). Thus we consider two types of models: those using initial volatile contents estimated from global compilations of melt inclusion studies (Wallace, 2005; Ruscitto et al., 2012) and those based on the formation of rhyolitic magmas by fractional crystallisation of a primitive basaltic melt (Appendix A). For basalts with 3 wt% water, 90% fractional crystallisation would result in rhyolites with over 30 wt% water. Such high volatile content is unlikely to be retained, therefore, we select a parameter range between the calculated values for rhyolite and the primitive basalt: 5-15 wt% H_2O; 1-3 wt% CO_2 and 1800-4200 ppm S (Supp. Table 1).

We chose the model starting depth by calculating the volatile saturation pressure for the specified composition and volatile content following the method of Liggins et al. (2022). We then decrease the pressure in a step-wise manner, calculating the mole fraction of exsolved volatiles for a number of species (e.g., H_2O, CO_2, SO_2, H_2S) at each step assuming closed-system degassing and thermodynamic equilibrium. From this, we can calculate the total gas fraction and magma density for a chamber at any given depth (Yip et al., 2022), and in Section 4, we then compare these general models to specific case studies where the chamber depth is known from geophysical or petrological constraints.

We assume the amount of exsolved SO_2 is equal to the co-eruptive SO_2 yield (Kilbride et al., 2016; Yip et al., 2022). In order to account for differences in eruption size, we define normalised SO_2 ($\bar{S}$) as the observed SO_2 emitted (E^{SO_2}), normalised by the volume of magma erupted (V_e; assuming dense-rock equivalent, DRE):

$$\bar{S} = \frac{E^{SO_2}}{V_e} = \frac{m^{SO_2} M^{SO_2} \rho_e w_g}{M_g}, \tag{1}$$

where m^{SO_2} is the mole fraction of SO_2 in gaseous phase, M^{SO_2} is the molecular mass of SO_2, ρ_e is the erupted rock density, w_g is the gas weight fraction, and M_g is the mean molecular mass of gas phase. In reality, co-eruptive exsolution and/or SO_2 scrubbing may modulate this value and these secondary processes are discussed further in Section 3.1.

We use the estimated magma density (ρ_m) to calculate the magma compressibility using the equation $\beta_m = \frac{1}{\rho_m}\frac{\delta\rho_m}{\delta p}$ (Rivalta and Segall, 2008). The normalised volume change during an eruption can then be denoted as $\bar{V}$:

$$\bar{V} = \frac{\Delta V_c}{V_e} = \left(1 + \frac{\beta_m}{\beta_c}\right)^{-1}, \tag{2}$$

where β_c is the compressibility of the chamber, which depends on its geometry and material properties (e.g. Amoruso and Crescentini, 2009; Yip et al., 2022). For our model simulations, we use $\beta_c = 10^{-10}$ Pa^{-1} for our initial models and explore this further in Section 2.3.

2.2. Effect of magma composition

Our goal is to apply this framework to understand global patterns of degassing and deformation, spanning the full range of eruption types and magma compositions. Here we conduct sensitivity tests for rhyolitic magmas, building on the work of Yip et al. (2022) who conducted similar tests for basaltic magmas. We then compare our results across the full range of magma compositions.

We explore the effects of varying the weight fraction of magmatic volatile content (w^{H_2O}, w^{CO_2}, w^S) and oxygen fugacity by performing one-at-a-time sensitivity tests, which vary a chosen parameter while keeping the other parameters constant (Fig. 1; Supp. Table 2). The sensitivity analysis reveals the role of each parameter on degassing and deformation, but does not consider the co-dependence of input variables, meaning some parameter combinations are not physically realistic.

The effects of varying w^{H_2O}, w^{CO_2}, w^S and f_{O_2} in rhyolitic magmas are similar to those reported by Yip et al. (2022) for basalts. Namely, 1) water-rich magmas generate higher $\bar{S}$ than water-poor magmas and are more compressible, meaning $\bar{V}$ is lower, 2) increasing S and f_{O_2} results in a higher $\bar{S}$, but these parameters have minimal impact on $\bar{V}$; and 3) increasing CO_2 causes a small increase in $\bar{S}$ and a small decrease in $\bar{V}$ (Fig. 1; Supp. Table 2). For comparison, we also show the model results using melt inclusions to determine the initial volatile content (red lines; Fig. 1). These are only applicable at depths 5 km and show a lower $\bar{S}$ and higher $\bar{V}$ due to the much lower volatile contents.

Next we compare our model results for 1) water-poor rhyolite (w^{H_2O} = 5.0 wt%) and 2) water-rich rhyolite (w^{H_2O} = 15 wt%) with the model results of Yip et al. (2022) for 3) water-poor basalts from ocean island settings (w^{H_2O} = 1.0 wt%) and 4) water-rich basalts from

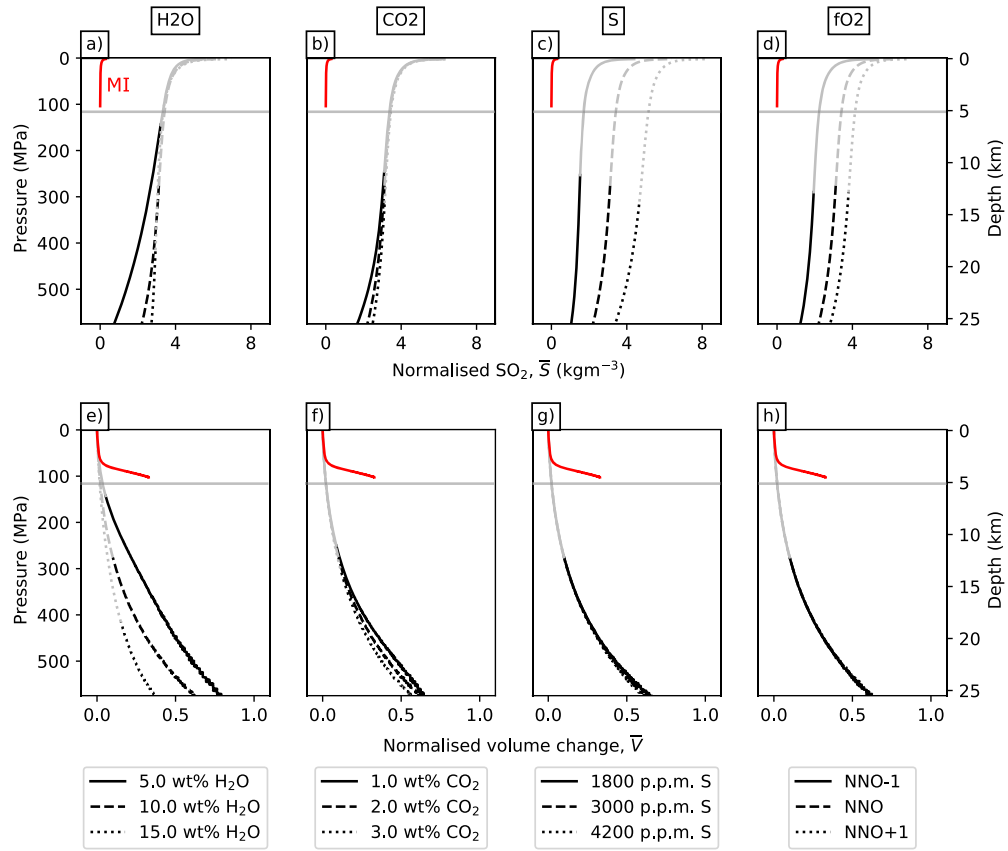

Fig. 1. Sensitivity tests showing the physicochemical properties of rhyolite when varying magmatic volatile content and oxygen fugacity. The observable parameters, namely (a-d) normalised SO_2 ($\bar{S}$) and (e-h) normalised volume change ($\bar{V}$), are shown when varying H_2O, CO_2, S and oxygen fugacity, while the rest of the parameters are kept constant. $\bar{S}$ and $\bar{V}$ calculated using melt inclusion data (MI) are shown as red lines. The grey lines in each panel represent magma properties after exceeding the percolation threshold, $\phi_c = 17$ vol%. Initial volatile contents are $w^{H_2O} = 10.0 \pm 5.0$ wt%, $w^{CO_2} = 2.0 \pm 1.0$ wt%, $f_{O_2} = \text{NNO} \pm 1$ and $w^S = 3000 \pm 1200$ ppm (Supplementary Table 1).

arc settings ($w^{H_2O} = 3.3$ wt%) (Fig. 2). Full details of the initial volatile contents are given in Supplementary Table 1. As expected, we find that both water-rich and water-poor rhyolites exsolve more H_2O and SO_2 gas than even the most water-rich basalts and hence produce greater $\bar{S}$ (Fig. 2a-c). Not only do the rhyolitic magmas have a higher initial sulfur content, the sulfur also preferentially partitions into the H_2O gas phase which forms at higher pressures in rhyolitic magmas (Fig. 2c). Since water content is the primary control on magma compressibility, rhyolitic magma, which contains more exsolved H_2O gas than basaltic magma (Fig. 2a), is more compressible and has lower $\bar{V}$ (Fig. 2f-h).

2.3. Effect of chamber compressibility

Chamber compressibility can vary over orders of magnitude depending on crustal material properties and chamber geometry (Rivalta and Segall, 2008; Anderson and Segall, 2011) and may also change over time due to fracturing and alteration (Carrier et al., 2015; Heap et al., 2020). Here we use our model to compare the relative effects of magma compressibility and chamber compressibility on volume change. We use the model of Heap et al. (2020) to estimate realistic elastic moduli for intact and fractured host rocks at depths of 2-10 km (Fig. 3a). Assuming a spherical or prolate reservoir, this gives chamber compressibilities in the range 6.0×10^{-11} Pa^{-1} $< \beta_c < 3.3 \times 10^{-10}$ Pa^{-1}, but oblate reservoirs are less compressible with values as high as $\beta_c = 1.6 \times 10^{-8}$ Pa^{-1} (Fig 3b). This range is similar to the range of magma compressibilities at similar depths (1.5×10^{-10} Pa^{-1} $< \beta_m < 2.0 \times 10^{-8}$ Pa^{-1}). We then use these values to calculate the ratio $\frac{\beta_c}{\beta_m}$ and $\bar{V}$ for the range of magma compositions and volatile contents considered in Section 3.2 (water-rich rhyolites, water-rich basalts, water-poor rhyolites and water-poor basalts). The results show that the normalised volume change is equally sensitive to variations in magma compressibility and chamber compressibility over realistic ranges, and both must be considered when analysing individual case studies (Fig. 3c,d).

3. Pre-eruptive gas segregation

3.1. Conceptual model

The terms 'open' and 'closed' are often used to describe simple conceptual models of volcanic behaviour, but are used by different communities in different ways (e.g., Newhall, 2007; Chaussard et al., 2013; Burgisser et al., 2015). When applied to degassing processes, the terms 'open' and 'closed' describe whether the exsolved volatiles remain in contact and in equilibrium with melt or not (e.g., Burgisser et al., 2015). For closed degassing, exsolved volatiles remain in physical contact with the melt and propagate at the same speed, while open degassing implies that exsolved volatiles are removed instantaneously (Burgisser et al., 2015). When applied to volcanic systems, the term 'closed' means that the system is sealed: no gas can escape from the reservoir (i.e., gas accumulates) and deformation may occur due to the build-up of pressure. Conversely, open volcanic systems may allow outgassing without observable deformation (Chaussard et al., 2013) (Fig. 4b-c). In reality, most volcanoes show time-varying behaviour including elements of both open- and closed-systems and degassing processes (Reath et al., 2019).

Here, we use the term 'pre-eruptive gas accumulation' to refer to open degassing in a closed volcanic system - exsolved volatiles segregate from the melt and accumulate in shallow reaches of the reservoir,

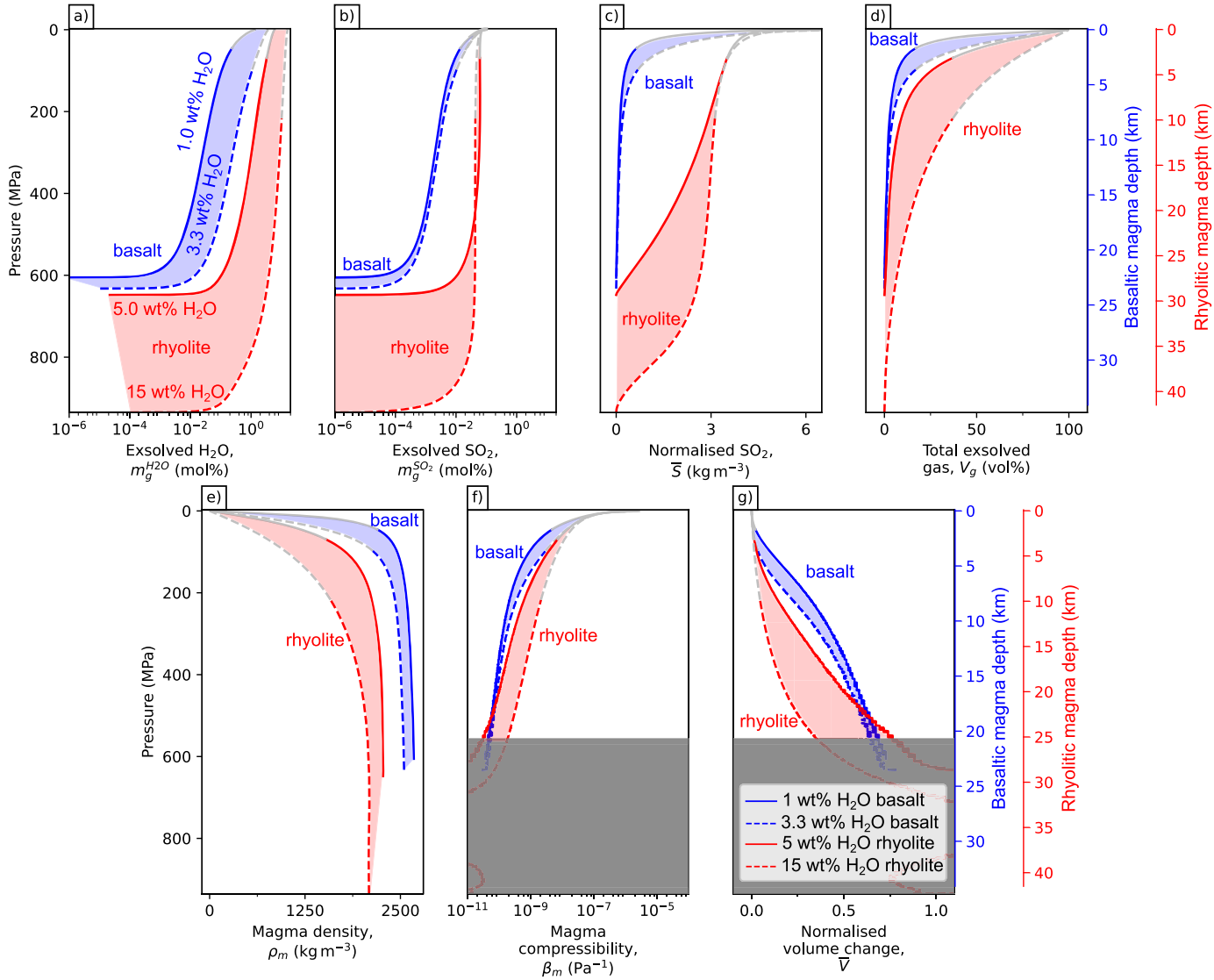

Fig. 2. Comparison of model predictions for basaltic eruptions (blue) and rhyolitic eruptions (red), and water-poor (full line) and water-rich (dashed line) compositions. Initial volatile contents are listed in Supplementary Table 1. Mole fraction of exsolved (a) H_2O and (b) SO_2 in gas phase. (c) Mass of SO_2 gas per unit volume of magma, also defined as normalised SO_2 ($\bar{S}$). (d) Volume fraction of exsolved gases in magma (V_g). (e) Magma density (ρ_m). (f) Magma compressibility (β_m). (g) Model predicted volume change normalised by unit volume of magma ($\bar{V}$). Depths below 580 MPa for panels f-h are shaded due to fluctuations in magma density at high pressures. The grey lines represent magma properties after exceeding the percolation threshold: $\phi_c = 17$ vol% for rhyolites and $\phi_c = 37$ vol% for basalts. The grey shaded area in panel f-g are to mask out erroneous results caused by the fluctuations in density gradient at high pressure due to numerical artefacts during modelling. Additionally, the modelling results for magma compressibility and normalised volume change at such depths (20 and 25 km for basalt and rhyolite respectively) would not be very reliable.

forming a gas-rich cap (Fig. 4b). We use 'pre-eruptive degassing' to refer to open degassing in an open volcanic system whereby exsolved volatiles are removed entirely (also called 'passive degassing') (Fig. 4c). We use the term 'co-eruptive degassing' to describe an effusive eruption where magma rises sufficiently slowly from the reservoir to the surface that additional exsolution and open degassing occurs during the eruption itself (Fig. 4e). During an explosive eruption, we assume that no additional volatiles exsolve during magma ascent and that the volatiles are in equilibrium with reservoir pressure (Fig. 4d). However, we note that volatiles can continue to exsolve to a certain extent during explosive eruptions. For instance, despite the explosive nature of the 2011 eruption of Grimsvötn, the volatile content in the groundmass is observed to be less than that in melt inclusions (Sigmarsson et al., 2013). This means that our model may underestimate the normalised SO_2 of an eruption if we were to extract the calculated value at reservoir depth. This is further discussed in Section 4.2 as we model SO_2 emissions as a function of depth. In both cases, secondary processes including high-temperatures gas-fluid, gas-magma and gas-rock interactions may reduce the observed SO_2 emissions (Symonds et al., 2001; Casas et al., 2019).

The efficiency by which exsolved volatiles can outgas from magmatic systems is governed by permeability and pore connectivity (Colombier et al., 2017). To the first-order, the transition between closed- and open-system degassing occurs at a critical porosity, called the percolation threshold (ϕ_c), which depends on the pore size distribution, ground mass crystallinity, degree of deformation and vesiculation processes amongst others (Colombier et al., 2017, 2020). The resulting wide range and natural variability in percolation thresholds prevents us incorporating these concepts directly in our numerical models. However, Colombier et al. (2020) identify two distinct regimes - at low melt viscosity or low gas overpressure, viscous bubble growth dominates and the percolation thershold, $\phi_c > 0.37$, whereas at high viscosity or high

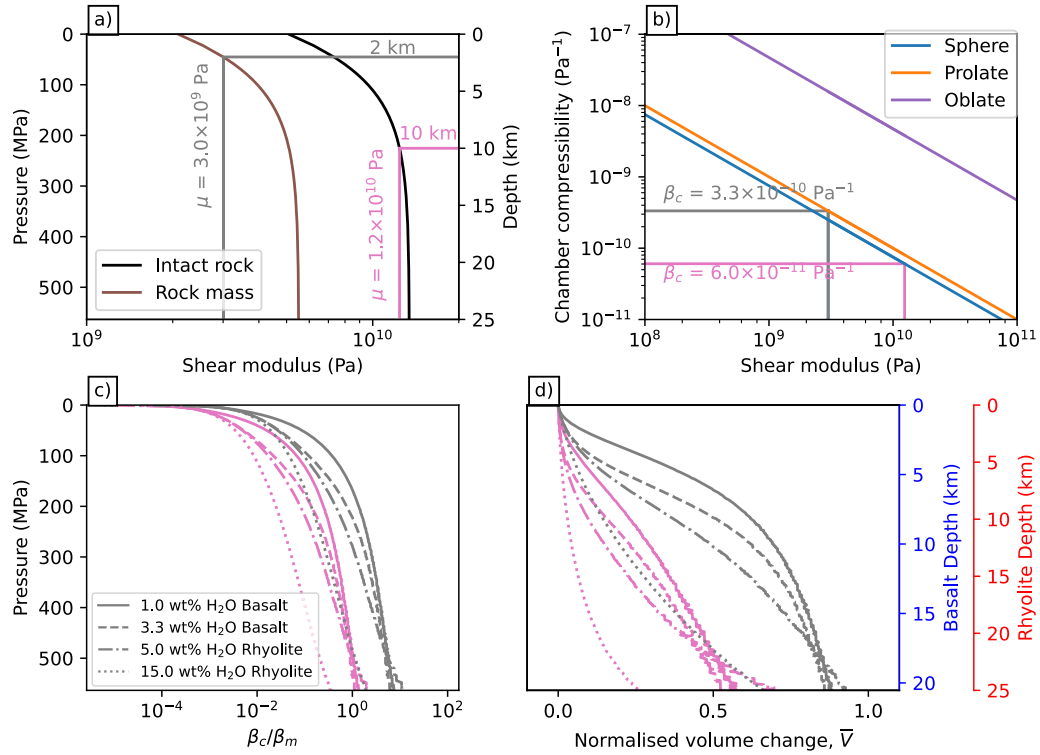

Fig. 3. Sensitivity tests showing the effects of chamber compressibility on deformation. (a) Crustal shear modulus as a function of depth calculated using the model of Heap et al. (2020) for intact rocks and the rock mass. (b) The chamber compressibility as a function of shear modulus for different geometries calculated using the equations from Anderson and Segall (2011). (c) The ratio of chamber to magma compressibility ($\frac{\beta_c}{\beta_m}$) and (d) $\bar{V}$ for the range of magma compositions and volatile contents, which are listed in Supplementary Table 1.

gas overpressure systems, fracture-driven processes dominate and the percolation threshold is much lower $\phi_c \sim 0.17$. Therefore, we indicate the point at which the gas volume fraction (V_g) reaches the percolation threshold of $\phi_c = 0.17$ using grey lines in Figs. 1, 2 and 5.

3.2. Modelling gas segregation

To model magmatic systems where the gas segregates from the melt and either accumulates in certain areas or degases prior to eruption, we adjust the gas volume fraction (V_g) calculated by EVo and consider the effect on magma density and compressibility. We use a proportion, k, to calculate the gas volume fraction accounting for pre-eruptive exsolved volatile accumulation or loss from magma (V_g'):

$$V_g' = V_g + k\,V_g. \tag{3}$$

Positive k represents pre-eruptive gas accumulation, while negative k represents pre-eruptive degassing, where k is always $-1 < k < 0$. Magma density (ρ_m) is the weighted average of the volatile-free magma density (ρ_M) and the gas density (ρ_g):

$$\rho_m = \rho_M(1 - V_g) + \rho_g\,V_g. \tag{4}$$

The magma density with varying gas content (ρ_m') can then be calculated by combining Equation (3) and (4) (see also Appendix B):

$$\rho_m' = \frac{\rho_M + V_g[\rho_g(1+k) - \rho_M]}{1 + k\,V_g}. \tag{5}$$

3.3. Model results

We use this model to explore the effects of pre-eruptive gas accumulation and degassing on magma properties and co-eruptive observations of $\bar{S}$ and $\bar{V}$ (Fig. 5). We vary k from −1 to +1 and use the default parameters of $w^{H_2O} = 10.0$ wt%, $w^{CO_2} = 2.0$ wt%, $w^{S} = 3000$ ppm and f_{O_2} = NNO. For $k = +1$, the gas volume, V_g', is twice that predicted by a closed system model ($k = 0$) and $\bar{S}$ is also doubled (Fig. 5b-c). The additional volume of exsolved gas reduces the magma density (up to a maximum of 26% at 4.4 km depth) and increases compressibility (up to a maximum of 73% at 11.5 km depth) (Fig. 5d-e) which reduces $\bar{V}$ by up to 27% at 20.4 km depth (Fig. 5f-g). For magmas with even higher values of k, the gas content exceeds the percolation threshold of 17 vol% (Colombier et al., 2021) and although our model predicts a highly compressible magma with very low $\bar{V}$, this is unlikely to be physically realistic.

For $k = -0.5$ (partial degassing), $\bar{S}$ and V_g are lower than for closed-system degassing. The reduced magma compressibility increases $\bar{V}$ up to a maximum of ~ 30% at 16.2 km (Fig. 5f-g). A completely degassed magma ($k = -1$) will have no gas content, and hence produce no emissions ($\bar{S} = 0$; Fig. 5b-c). However, because completely degassed magma is denser than the volatile-rich magma at depth (Fig. 5d) (Stevenson and Blake, 1998), magma density (ρ_M) actually increases with decreasing pressure (< 25 km). Consequently, we cannot use this model to estimate compressibility when k <-0.8 (Fig. 5e-g) (Supp. Table 2).

4. Comparison to observations

In this section, we compile observations of ground deformation, SO_2 emissions, volume of magma extruded and reservoir depth for eruptions with a range of magma compositions and compare them to our model results. The goal is to understand pre- and co-eruptive degassing processes and their implications for interpreting volcano monitoring data.

4.1. Data compilation

Earth-observing satellite missions are now providing global and frequent measurements of volcanic activity, including deformation and SO_2 degassing (Carn, 2016; Furtney et al., 2018; Ebmeier et al., 2018),

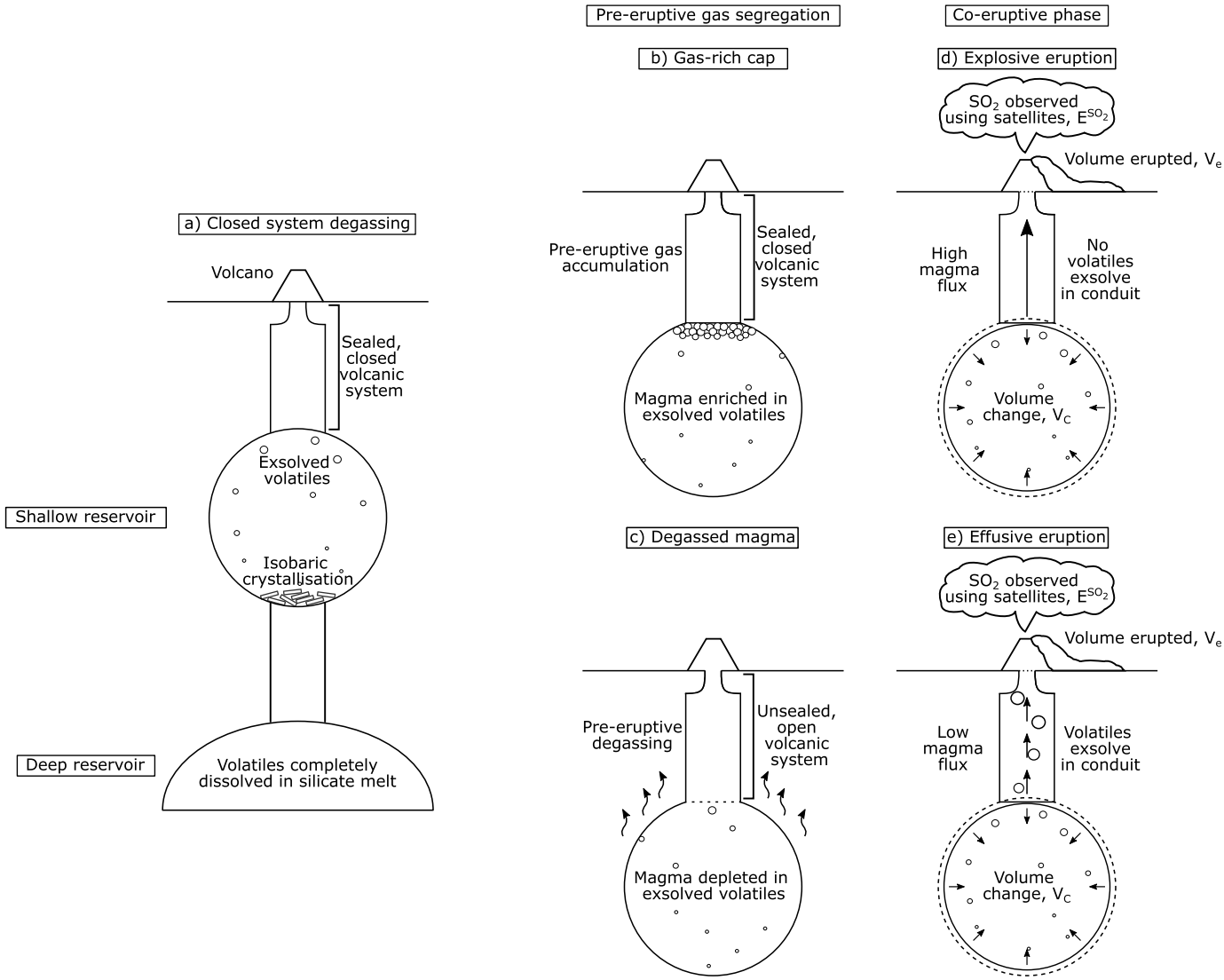

Fig. 4. Conceptual model of gas segregation within magmatic system. (a) Volcano with chambers at different depths. Magmatic volatiles are highly soluble in deep magmatic chambers and thus remain dissolved in the silicate melt. In the shallow chamber, volatiles exsolve during closed system degassing and/ or isobaric crystallisation. (b) A closed volcanic system in which the exsolved gas phase segregated from the melt rises buoyantly and accumulates in the roof zone of a magma reservoir. (c) An open volcanic system with interconnected permeable pathways that allows magma outgassing, removing exsolved volatiles from the reservoir. (d) Explosive eruptions with rapid magma removal and decompression, which results in little volatile exsolution during magma ascent. (e) Effusive eruptions have a low magma ascent rate between the chamber and the surface, allowing volatile exsolution in the conduit, i.e., co-eruptive degassing.

while erupted volume can be estimated from many different methods depending on deposit type (Galetto et al., 2023). However, each measurement type has limitations in terms of spatial and temporal resolution meaning that surprisingly few eruptions have measurements of all three parameters required to estimate $\bar{V}$ and $\bar{S}$, namely volume change, SO_2 emissions and volume erupted. Therefore, we start with the compilation of Kilbride et al. (2016) which lists 'sulfur yield' which is equal to $\bar{S}$ and the ratio, $r = {}^{1}/_{\bar{V}}$, for 11 eruptions. We then expand this dataset by conducting a literature search for additional datapoints based on the Global Volcanism Program (2013) catalogue.

We identified 20 eruptions with known erupted volume and source depth and measurements of co-eruptive SO_2 degassing or deformation (Fig. 6). Table 1 provides an overview with detailed descriptions provided in Supplementary Tables 3-9. Magma compositions are taken from published geochemical studies and divided into two categories: silica-poor eruptions ($SiO_2 < 50$ wt%) and silica-rich eruptions ($SiO_2 > 50$ wt%) (Fig. 6). Eruption volumes range from 10^7-10^9 m^3 and are collated from published studies using a range of techniques including photogrammetry, digital elevation models and analyses of tephra fall deposits (e.g., Romero et al., 2016; McKee et al., 2021; Galetto et al., 2023). SO_2 measurements are available for all the eruptions using space-borne spectrometers (e.g., Carn, 2016; Ge et al., 2016), except for the 2004 eruption of Mount St. Helens, USA. Volume change estimates are available for 13 eruptions, of which 8 are from InSAR and 5 from GPS (e.g., Hreinsdóttir et al., 2014; Hotta et al., 2019). Reservoir depths are primarily based on geodetic and seismic data, but petrological estimates are used where no geophysical measurements were available (Supp. Table 7). All depths are equivalent to pressures of less than 300 MPa, compatible with the sulfide and sulfate capacity laws used in our thermodynamic model, EVo (Liggins et al., 2020) with the exception of the 2010 eruption of Merapi.

Ideally, our compilation would also include estimates of chamber compressibility on a case-by-case basis. Of the 20 examples in our compilation, 12 have point or prolate sources, 7 are unknown or complex geometries and only 1 is sill-like (Fig. 7). However, insufficient information is available on aspect ratios or material properties to calculate individual chamber compressibilities so we consider end member values of chamber compressibility of 6×10^{-11} Pa^{-1} and 3.3×10^{-10} Pa^{-1}

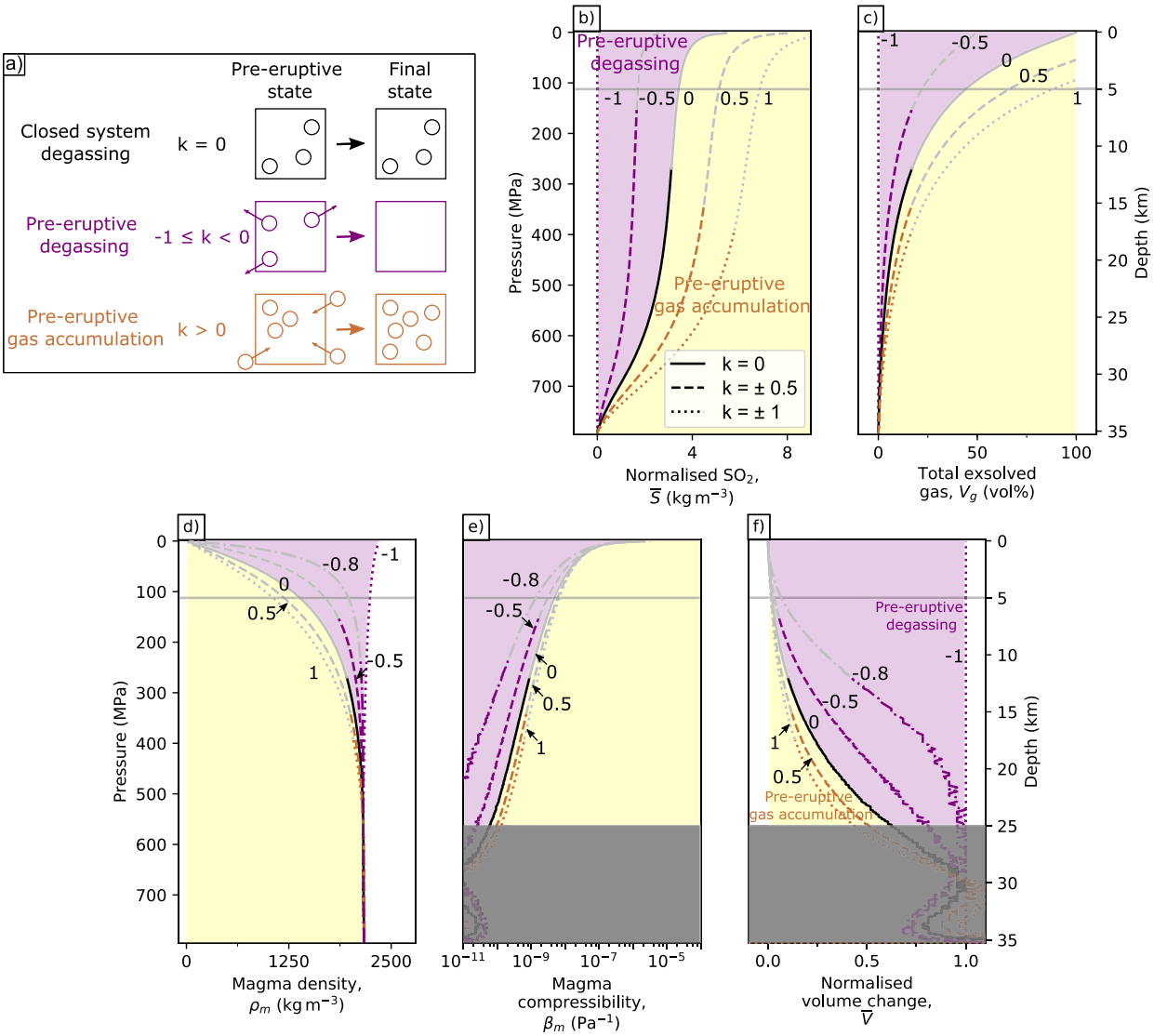

Fig. 5. Model predictions considering pre-eruptive gas segregation processes. (a) Conceptual model of pre-eruptive volatile segregation, where constant k represents volatile segregation processes. Positive k represents pre-eruptive gas accumulation and negative k, such that $-1 < k < 0$, represents pre-eruptive degassing. (b-g) Magma properties of rhyolite with pre-eruptive volatile segregation. $k = 0.8$ is included in panel d-g. The grey lines represent magma properties after exceeding percolation threshold $\phi_c = 17$ vol%. Fixed parameters: $w^{H_2O} = 10.0$ wt%, $w^{CO_2} = 2.0$ wt%, $w^S = 3000$ ppm. Explanation for grey shaded area is in Fig. 2.

based on Fig. 3. These assumptions affect the interpretation of individual systems, but should not affect our overall conclusions (Fig. 8).

4.2. Sulfur dioxide, $\bar{S}$

Observations of $\bar{S}_{obs}$ from silica-poor eruptions (SiO_2 < 50 wt%) range from <1 kg m^{-3} for the 2007 eruption of Piton de la Fournaise, France, to 9 kg m^{-3} at the 2019 eruption of Raikoke, Japan (Fig. 6b,d,f). The total mass of SO_2 emitted is consistent with model predictions for source depths of <2 km even though the reservoirs are at depths of more than 4 km (Fig. 7a). We attribute this to co-eruptive degassing between the reservoir and the surface, consistent with the low sulfur contents of basaltic lava flows (e.g., Sigmarsson et al., 2013; Donovan et al., 2018). In contrast, there is little evidence for co-eruptive degassing in silica-rich eruptions (SiO_2 > 50 wt%), which have $\bar{S}_{obs}$ <5 kg m^{-3} and do not cluster around the 0-2 km interval of the model predictions (Fig. 7b). Co-eruptive degassing preferentially occurs in mafic magmas due to 1) the high temperature, which causes high volatile diffusivity (Baker et al., 2005), and 2) the slow ascent rate of effusive eruptions (Gonnermann and Manga, 2006).

In Fig. 7c,d we compare the observations of silica-rich eruptions (SiO_2 >50 wt%) to the model predictions. We estimate initial H_2O and CO_2 content using the model of fractional crystallisation and a broad range of initial sulfur contents to represent natural variability (1800-4200 ppm). Six of the silica-rich eruptions have $\bar{S}_{obs}$ in the range predicted by the closed-system model (Fig. 7c) but the other six lie close to the $k = -1$ line, consistent with almost complete pre-eruptive outgassing (Fig. 7d). However, all the observed eruptions have $\bar{S}_{obs}$ greater than the model predictions when initial volatile contents are estimated from melt inclusions (Fig. 7b-c), consistent with the presence of a gas phase (e.g., Wallace and Gerlach, 1994; Wallace et al., 1995).

4.3. Volume change, $\bar{V}$

Measurements of normalised volume change, $\bar{V}_{obs}$, range from 0.03 to 0.74 with generally lower values for silica-rich eruptions at comparable depths, consistent with higher initial volatile contents (Fig. 6a,c,e). Both silica-rich and silica-poor categories show a broad trend with larger $\bar{V}_{obs}$ for deeper reservoirs and smaller $\bar{V}_{obs}$ for shallower reservoirs. This is consistent with closed-system behaviour: shallower reser-

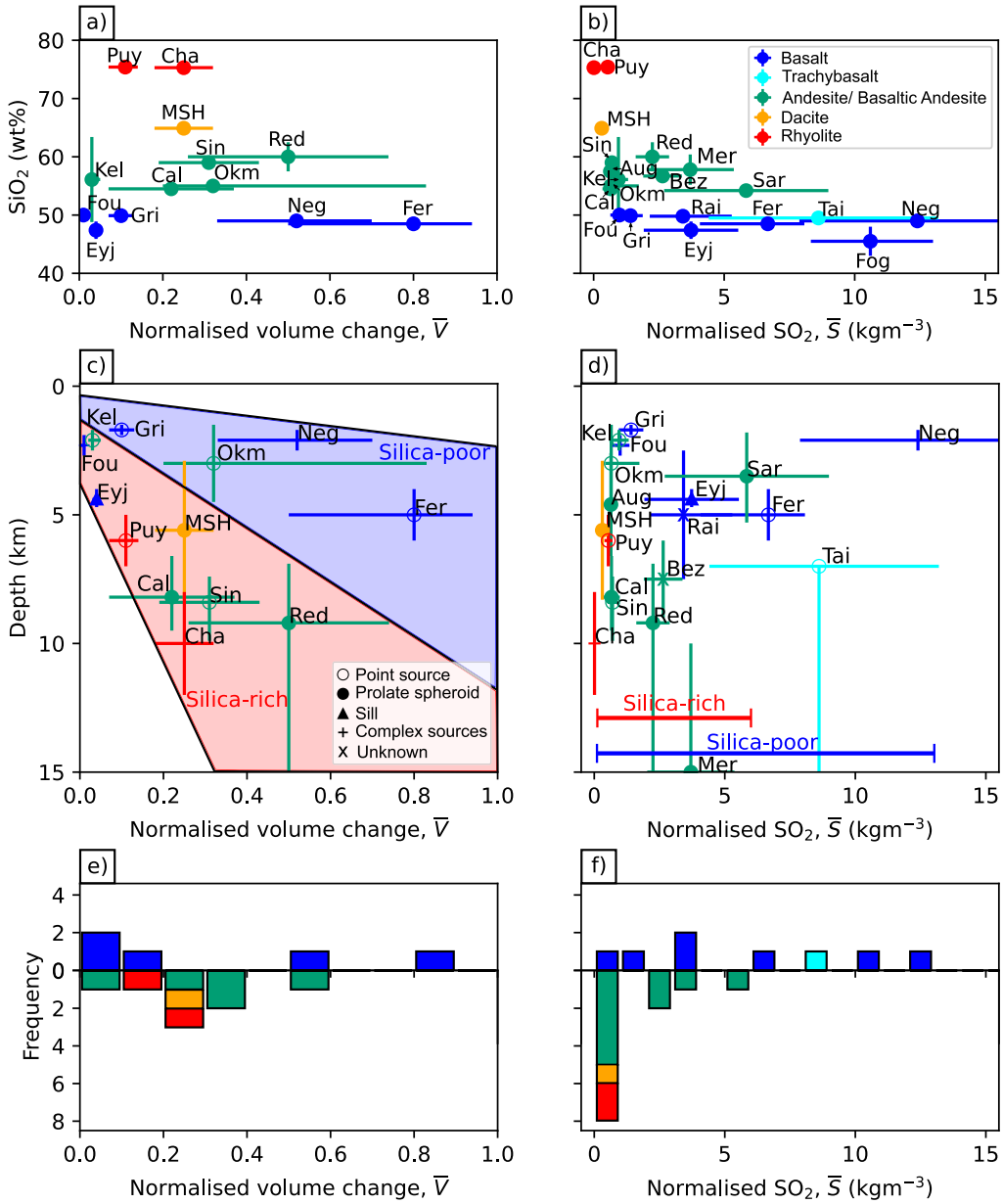

Fig. 6. Observations of deformation and SO_2 degassing from 20 eruptions between 2005-2021 (Supp. Table 3-9). The compilation consists of co-eruptive volume change and SO_2 gas emissions, both normalised by the erupted volume. (a-b) Normalised volume change ($\bar{V}_{obs}$) and normalised SO_2 ($\bar{S}_{obs}$) as a function of SiO_2 content. The colours are defined using the GVP classifications and correspond to the following ranges of SiO_2 content: basalt 45-52 wt%; basaltic andesite-andesite 52-63 wt%; dacite 63-70 wt%; rhyolite >70wt%. (c-d) Normalised volume change ($\bar{V}_{obs}$) and normalised SO_2 ($\bar{S}_{obs}$) as a function of reservoir depth. Shaded regions represent the range of observations. (e-f) Frequency plot for $\bar{V}_{obs}$ and $\bar{S}_{obs}$. All data points are colour-coded for magma composition, and the different symbols represent the different reservoir geometry. Data are shown for the following eruptions: (Aug) Augustine, 2006; (Bez) Bezymianny, 2007; (Cal) Calbuco, 2015; (Cha) Chaitén, 2008; (Eyj) Eyjafjallajökull, 2010; (Fer) Fernandina, 2005; (Fog) Fogo, 2014; (Fou) Piton de la Fournaise, 2007; (Gri) Grímsvötn, 2011; (Kel) Kelut, 2014; (Mer) Merapi, 2010; (MSH) Mount St. Helens 2004; (Neg) Sierra Negra, 2005; (Okm) Okmok, 2008; (Puy) Puyehue-Cordón Caulle, 2011; (Rai) Raikoke, 2019; (Red) Redoubt, 2009; (Sar) Sarychev Peak, 2009; (Sin) Sinabung, 2013; (Tai) Jebel at Tair, 2007.

voirs are more gas-rich and compressible and hence produce less deformation per unit volume erupted (Kilbride et al., 2016; Yip et al., 2022). However, the scatter suggests that other factors modulate the relationship, such as magmatic volatile content, pre-eruptive gas segregation and chamber compressibility.

In Fig. 7e, we compare observations of silica-poor eruptions $SiO_2 <$ 50 wt% to the model predictions for basaltic magmas with a range of water contents (1-3.3 wt% H_2O) and chamber compressibilities (6×10^{-11} Pa^{-1}; 3.3×10^{-10} Pa^{-1}). Three of the eruptions have a higher $\bar{V}_{obs}$ than expected, even for water-poor basalts and high chamber compressibilities, indicating the magma is less compressible than can be explained using a closed-system model (Fig. 7e). Fig. 7f shows that these eruptions lie in the $-1 < k < 0$ domain indicating that the magma was partially depleted by outgassing prior to eruption, consistent with observations of passive degassing at mafic volcanoes (e.g., Barry et al., 2014; Carn et al., 2016). The other two eruptions have lower $\bar{V}_{obs}$ and can either be explained by a low chamber compressibility or pre-eruptive gas accumulation. In the case of the 2010 eruption of Eyjafjallajökull, Iceland, previous studies have suggested that some magma was sourced from a deeper reservoir and hence the co-eruptive volume change is an underestimate (Sigmundsson et al., 2010).

In Fig. 7g, we compare the observations of silica-rich eruptions (SiO_2 > 50 wt%) to the model predictions using initial H_2O contents of 5 and 15 wt% H_2O from the model of fractional crystallisation (Table 1) and chamber compressibilities of 6×10^{-11} Pa^{-1} and 3.3×10^{-10} Pa^{-1} (Fig. 3). For roughly half of the eruptions, $\bar{V}_{obs}$ lies within the range predicted for closed-system degassing of a chamber with high compressibility (Fig. 7g), while the others have $\bar{V}_{obs}$ greater than the predictions for even water-poor rhyolite and high chamber compressibility and lie in the pre-eruptive outgassing regime (Fig. 7h). However, all but one of the observations can be explained by closed-system degassing, if we use a lower initial water content of 3.3 wt% based on melt inclusion studies (Fig. 7g).

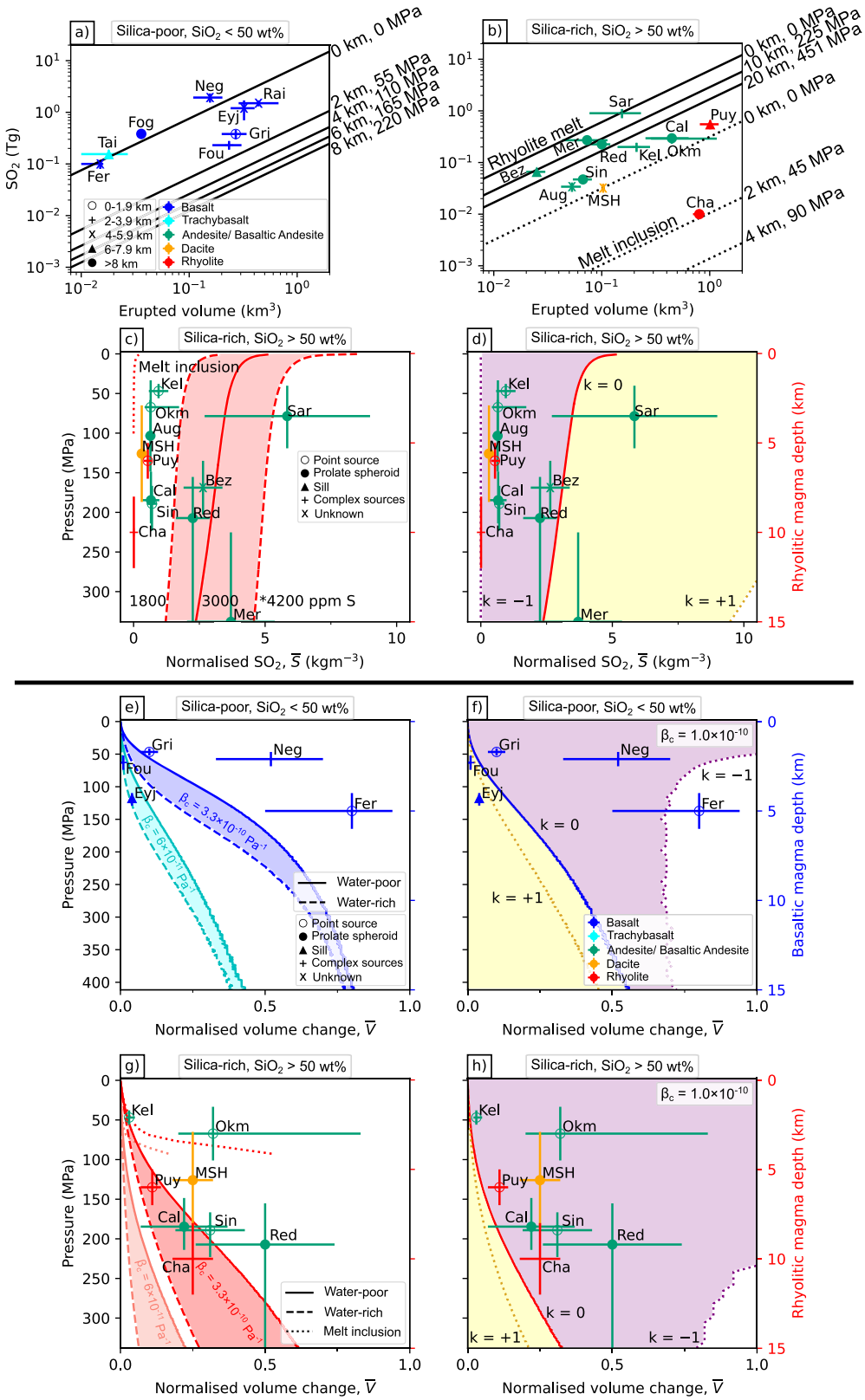

Table 1
Compilation of observations of normalised volume change, $\bar{V}_{obs}$, and normalised SO_2, $\bar{S}_{obs}$, source depth and magma composition for 20 recent eruptions. Further details are provided in Supplementary Tables 3-9.

Volcano	Eruption Date	SiO_2 wt%	Depth km	$\bar{V}_{obs}$	$\bar{S}_{obs}$ Tg km^{-3}
Augustine, USA	Jan 2006	57.5 ± 1.5	$4.6^{6.6}_{2.6}$		$0.64^{0.82}_{0.55}$
Bezymianny, Kamchatka	Oct 2007	56.7 ± 0.2	$7.5^{9.0}_{6.0}$		$2.64^{3.38}_{1.90}$
Calbuco, Chile	Apr 2015	54.5 ± 0.5	$8.2^{9.5}_{6.6}$	$0.22^{0.37}_{0.07}$	$0.66^{0.98}_{0.34}$
Chaitén, Chile	May 2008	75.3 ± 0.3	$10^{12}_{8.0}$	$0.25^{0.32}_{0.18}$	$0.01^{0.02}_{0.01}$
Eyjafjallajökull, Iceland	Apr-May 2010	47.4 ± 1.5	$4.4^{4.7}_{4.0}$	$0.04^{0.05}_{0.03}$	$3.73^{5.54}_{1.92}$
Fernandina, Galapagos	May 2005	48.5 ± 0.5	$5.0^{6.0}_{4.0}$	$0.80^{0.94}_{0.50}$	$6.67^{8.07}_{4.07}$
Fogo, Cape Verde	Nov 2014-Feb 2015	45.5 ± 2.5	16.5		$10.6^{13.0}_{8.32}$
Grimsvötn, Iceland	May 2011	49.9 ± 0.8	$1.7^{1.9}_{1.5}$	$0.10^{0.13}_{0.07}$	$1.41^{1.88}_{0.94}$
Kelut, Indonesia	Feb 2014	56.1 ± 7.3	$2.1^{2.5}_{1.7}$	$0.03^{0.05}_{0.02}$	$0.95^{1.32}_{0.58}$
Merapi, Indonesia	Nov 2010	57.8 ± 2.6	15^{20}_{10}		$3.70^{5.37}_{2.03}$
Mount St. Helens, USA	2004-2008	64.9 ± 0.1	$5.6^{8.3}_{2.9}$	$0.25^{0.32}_{0.18}$	$0.31^{0.37}_{0.25}$
Sierra Negra, Galapagos	Oct 2015	49.0 ± 0.9	$2.1^{2.5}_{1.7}$	$0.52^{0.70}_{0.33}$	$12.4^{16.9}_{7.88}$
Okmok, USA	Jul-Aug 2008	55.0 ± 0.3	$3.0^{4.5}_{1.5}$	$0.32^{0.83}_{0.20}$	$0.65^{1.73}_{0.42}$
Piton de la Fournaise, France	Mar-Apr 2007	50.0 ± 0.4	$2.3^{2.7}_{1.9}$	$0.01^{0.02}_{<0.01}$	$0.99^{1.35}_{0.64}$
Puyehue-Cordón Caulle, Chile	Jun 2011	75.4 ± 0.7	$6.0^{7.0}_{5.0}$	$0.11^{0.14}_{0.07}$	$0.54^{0.70}_{0.39}$
Raikoke, Kuril Islands	Jun 2019	49.8 ± 0.5	$5.0^{7.5}_{2.5}$		$3.42^{5.29}_{2.15}$
Redoubt, USA	Mar-Apr 2009	60.0 ± 2.5	$9.2^{15.2}_{6.9}$	$0.50^{0.74}_{0.26}$	$2.25^{2.89}_{1.61}$
Sarychev Peak, Kuril Islands	Jun 2009	54.2 ± 0.2	$3.5^{5.3}_{1.8}$		$5.84^{8.99}_{2.70}$
Sinabung, Indonesia	Dec 2013-Apr 2014	59.0 ± 0.3	$8.4^{9.9}_{7.4}$	$0.31^{0.43}_{0.19}$	$0.70^{0.89}_{0.51}$
Jebel al Tair, Saudi Arabia	2007-2008	49.5 ± 0.6	$7.0^{15}_{7.0}$		$8.61^{13.2}_{4.41}$

4.4. Combining $\bar{V}_{obs}$ and $\bar{S}_{obs}$

Interestingly, although our compilations of $\bar{V}_{obs}$ and $\bar{S}_{obs}$ both indicate that many volcanoes experience pre-eruptive outgassing, the measurements are not consistent for individual volcanoes (e.g., $\bar{V}_{obs}$ may be in the pre-eruptive outgassing regime but $\bar{S}_{obs}$ is in the pre-eruptive gas accumulation regime or vice versa). This apparent discrepancy can be explained by the heterogeneity in sulfur concentration in the melt and uncertainties in SO_2 detection. For example, the 2008 eruption of Chaitén, Chile lies in the predicted range for $\bar{V}$, but not $\bar{S}$, and the anomalously low SO_2 emissions have previously been explained by SO_2 scrubbing (Carn et al., 2016; Casas et al., 2019).

5. Discussion

This study provides new insights into the influence of pre-eruptive magma storage conditions and co-eruptive processes on observations of volcanic deformation and degassing. We use numerical models to investigate the role of reservoir depth, water content, sulfur content, chamber compressibility and pre-eruptive gas segregation on observations of volcanic deformation and SO_2 emissions. The models predict that reservoir depth, chamber compressibility and magma composition will have first-order controls, but that gas segregation processes will also have a significant impact.

Our compilation of eruption data confirms the first-order trend between normalised volume change and reservoir depth, such that shallow reservoirs produce small volume changes. While this is qualitatively consistent with a model of closed-system degassing in which shallow reservoirs contain gas-rich, compressible magma, the scatter suggests that other factors modulate the volume changes of the reservoir, namely magmatic water content and pre-eruptive gas segregation.

Comparison to model predictions suggests that all magmatic systems undergo a certain degree of outgassing prior to an eruption. For evolved magmas, the amount of degassing is similar to or lower than expected if we assume closed system fractional crystallisation, but greater than expected if we only consider the dissolved volatile content preserved in melt inclusions. This is consistent with the model of a transcrustal magmatic system, in which exsolved gas separates from the melt and rises buoyantly to accumulate in different parts of the system. Thus, the gas content of the reservoir from which the magma erupted may be gas-rich compared to predictions based on melt-inclusion data and also partially depleted in gas compared to predictions based on fractional crystallisation. We also find that mafic eruptions typically experience co-eruptive degassing, producing relatively large amounts of SO_2 per volume erupted despite their low magmatic sulfur content. However, considering the input parameters represents that of a generic basalt and rhyolite, it is also important to acknowledge that the normalised SO_2

Fig. 7. Comparison between model predictions and observations of (a-d) SO_2 degassing and (e-h) co-eruptive volume change (Supp. Table 3-9). The magma composition used for the models are that of a generic basalt and rhyolite, which are presets in EVo, and the volatile content used in the models has been listed in Supplementary Table 1. (a) Relationship between the erupted volume (dense-rock equivalent, DRE) and the total mass of SO_2 released for eruptions with $SiO_2 < 50$ wt%. The diagonal lines are modelled using an ocean island basalt composition ($w^{H_2O} = 1.0$ wt%, $w^{CO_2} = 1.0$ wt%, f_{O_2} = NNO and $w^S = 1600$ ppm; Supp. Table 1) assuming a closed degassing system. (b) Same as panel a but for eruptions with $SiO_2 > 50$ wt%. The diagonal lines are modelled using magma composition of rhyolite formed by fractional crystallisation (5.0 wt% H_2O; full line) and melt inclusion data from typical rhyolitic magma (dotted line). (c) Normalised SO_2, $\bar{S}_{obs}$ for eruptions with $SiO_2 > 50$ wt% compared to model predictions using different sulfur content (full and dashed lines) and melt inclusions (dotted line) as a function of depth. (d) $\bar{S}_{obs}$ for eruptions with $SiO_2 > 50$ wt% compared to model predictions for 5 wt% H_2O rhyolite (full line), with dotted lines representing pre-eruptive exsolved volatile segregation, such that $k = +1$ represents pre-eruptive gas accumulation and $k = -1$ represents pre-eruptive degassing. (e) Normalised volume change $\bar{V}_{obs}$ of eruptions with $SiO_2 < 50$ wt% compared to model predictions for water-rich (dashed line) and water-poor basalts (full line) with chamber compressibilities of 6×10^{-11} Pa^{-1} and 3.3×10^{-10} Pa^{-1}. (f) $\bar{V}_{obs}$ of eruptions with $SiO_2 < 50$ wt% compared to model predictions for water-poor basalts (full line), with dotted lines representing pre-eruptive exsolved volatile segregation, such that $k = +1$ represents pre-eruptive gas accumulation and $k = -1$ represents pre-eruptive degassing. (g) $\bar{V}_{obs}$ of eruptions with $SiO_2 > 50$ wt% compared to model predictions for water-rich (15 wt% H_2O; dashed line), water-poor rhyolites (5.0 wt% H_2O; full line) and melt inclusions (dotted line) and chamber compressibilities of 6×10^{-11} Pa^{-1} and 3.3×10^{-10} Pa^{-1}. (h) $\bar{V}_{obs}$ of eruptions with $SiO_2 > 50$ wt% compared to model predictions for water-poor rhyolites that underwent closed-system degassing (full line) and pre-eruptive gas accumulation and degassing (dotted lines). See Fig. 5 for additional information on pre-eruptive exsolved volatile segregation. *In c, the water content is 5 wt% for the model run with a sulfur content of 1800 and 3000 ppm and 10 wt% for the model run with a sulfur content of 4200 ppm. All data points are listed in Table 1 and colour-coded for magma composition. The different symbols represent the different (a-b) reservoir depths and (c-h) reservoir geometry. Abbreviations are shown in Fig. 6.

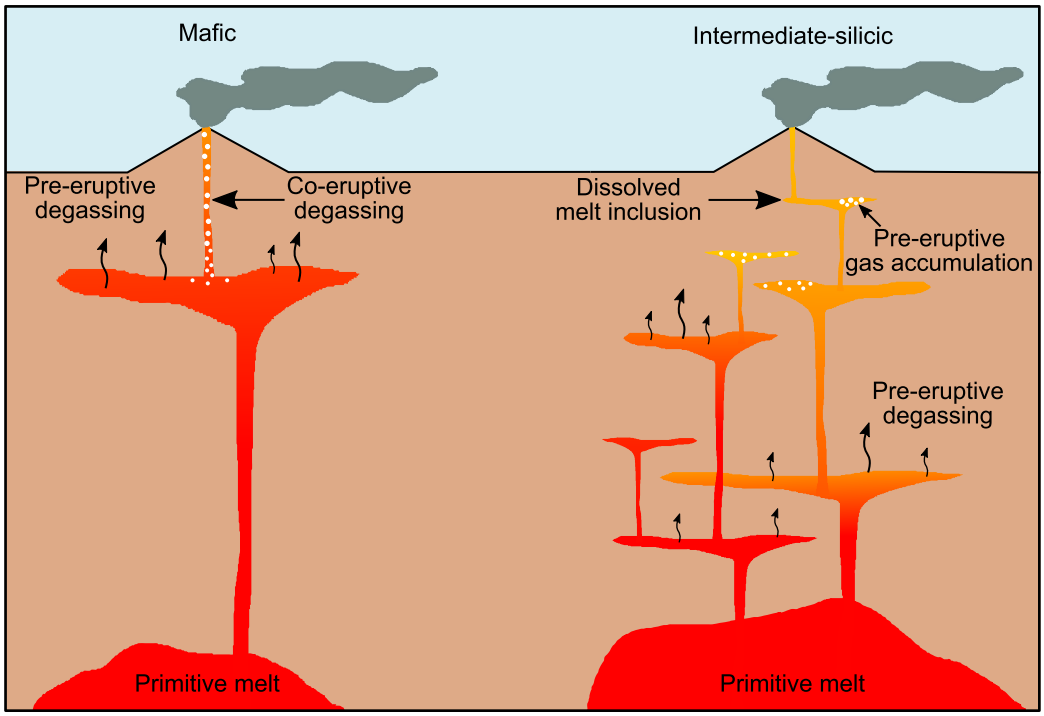

Fig. 8. Conceptual model comparing the magmatic systems feeding silica-rich and silica-poor eruptions. The colour gradient represents magma composition, with red representing primitive melt (i.e., least evolved) and yellow representing evolved, silicic magma. Silica-poor systems (left) have high volatile diffusivity due to high temperature, which allows co-eruptive degassing during magma ascent to the surface. Silica-rich systems (right) have complex transcrustal magmatic systems. Volatile enrichment occurs during the fractional crystallisation of the primitive melt. The volatiles exsolved may accumulate as gas-rich caps or be lost due to outgassing at different parts of the system. The reservoir from which an eruption occurs may therefore be gas-rich or gas-poor relative to the initial magmatic conditions and thus modify observations of co-eruptive volume change and degassing. A fraction of volatiles that is already exsolved may not be recorded in melt inclusion data, thereby underestimating the pre-eruptive gas content in the reservoir and total SO_2 emissions.

and normalised volume changes predicted by the model might exhibit discrepancies when compared to the actual data from specific eruptions.

However, these models are clearly oversimplified and our analysis is limited by a lack of suitable data. We were only able to identify 20 eruptions for which data was available on erupted volume, volume change and SO_2 emissions. Although satellite data now provides compilations of SO_2 emissions and surface deformation (Carn et al., 2016; Ebmeier et al., 2018), these are not provided on an operational basis and not all eruptions are included. To illustrate the challenge, we compared the three best currently-available catalogues: Galetto et al. (2023) for erupted volume, Ebmeier et al. (2018) for volcanic deformation and Carn (2016) for SO_2 emissions (Fig. 9). Ebmeier et al. (2018) compiled 308 deformation episodes between 1990-2015, of which 78 were related to an eruption. However, source depths were only provided for 45 of these eruptions and there is no information on volume change. Galetto et al. (2023) compiled 682 estimates of mass erupted between 1961-2020, which relates to 209 individual eruptions. Carn (2016) compiled estimates of SO_2 loading for 47 eruptions between 1979-2014. If we restrict these to the overlapping date range of 2005-2014, we are left with 48 eruptions from the Ebmeier et al. (2018) catalogue, 79 eruptions from the Galetto et al. (2023) catalogue and 29 eruptions from Carn (2016). However, of these, there are only 9 eruptions for which all three measurements are available: Chaitén, Chile 2008; Puyehue-Cordón Caulle, Chile, 2011; Sierra Negra, Galapagos, 2005; Tolbachik, Russia, 2012; Jebel at Tair, Saudi Arabia, 2007; Eyjafjallajökull, Iceland, 2010; Piton de la Fournaise, France, 2007 and Merapi, Indonesia, 2010.

Even less information is available about crustal shear modulus (μ). Seismic tomography can be used to estimate material properties, but is only available at a small number of well-studied volcanoes. For example, the compilation of Paulatto et al. (2022) only includes one of the volcanoes in our list: Merapi. Heap et al. (2020) provide a method of estimating depth-dependent rock mass Young's moduli for volcanic rocks; their empirical data is from room pressure or shallow tunnels and it is

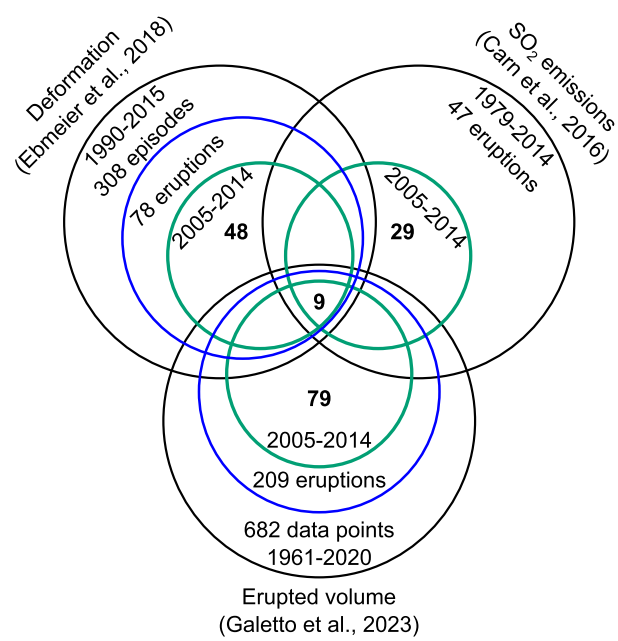

Fig. 9. Illustration of the three best currently-available catalogues for volcano monitoring: Galetto et al. (2023) for erupted volume, Ebmeier et al. (2018) for volcanic deformation and Carn (2016) for SO_2 emissions (Fig. 9). Each catalogue has a different observation period. With an overlapping date range of 2005-2014, there are only 9 eruptions for which all three measurements are available.

not yet clear whether the relationships are applicable to rock masses at depths greater than a few hundred metres.

6. Conclusions

This study provides new insights into the influence of pre-eruptive magma storage conditions and co-eruptive processes on observations of volcanic deformation and degassing. We use numerical models to investigate the role of reservoir depth, water content, sulfur content, chamber compressibility and pre-eruptive gas segregation on observations of volcanic deformation and SO_2 emissions. The models predict that reservoir depth, chamber compressibility and magma composition will have first-order controls, but that gas segregation processes will also have a significant impact.

Our analysis of silica-poor eruptions is consistent with a simple conceptual model of a single short-lived reservoir that undergoes some minor degassing prior to eruption, followed by an effusive eruption with significant degassing taking place between the reservoir and the vent (Fig. 8a). SO_2 emissions from mafic systems are dominated by co-eruptive degassing, meaning that mafic systems are big SO_2 gas emitters despite the fact that our analysis of volume change measurements shows that the reservoirs have undergone some pre-eruptive degassing.

In contrast, our analysis of eruptions involving silica-rich compositions is more consistent with current models of transcrustal magmatic systems (e.g., Cashman et al., 2017), in which the exsolved volatile phase may undergo pre-eruptive degassing or gas accumulation at various depths prior to an eruption (Fig. 8b). In this conceptual model, a fraction of the volatile content inherited from the primitive basalt is outgassed prior to the formation of melt inclusions, but subsequently, exsolved gas may accumulate as gas-rich caps. The complexity of the magma storage in silica-rich systems ultimately complicates the interpretation of volcanic deformation and SO_2 degassing (Fig. 8). Indeed, many andesitic eruptions alternate between explosive and extrusive phases suggesting that the gas content in the erupting magma varies during an eruption (e.g. Jaupart and Allègre, 1991; Cassidy et al., 2018).

Our results emphasise the need to reconcile multiparameter observations from different disciplines of volcanology (e.g., geophysics, geochemistry, petrology) when interpreting monitoring data. However, our analysis is limited by a lack of a systematic approach to collecting monitoring data (gas, deformation, volume) and basic characteristics (magma composition, crustal properties). Analyses that focus on a single data type are unable to obtain a full picture of the system and may be biased by assumptions. Thus further integration of multiparameter datasets with physical models is critical for understanding magmatic plumbing systems, as well as improve our understanding of monitoring data.

CRediT authorship contribution statement

Stanley Tze Hou Yip: Writing – review & editing, Writing – original draft, Visualization, Validation, Software, Project administration, Methodology, Investigation, Formal analysis, Data curation, Conceptualization. **Juliet Biggs:** Writing – review & editing, Validation, Supervision, Project administration, Methodology, Funding acquisition, Conceptualization. **Marie Edmonds:** Writing – review & editing, Validation, Supervision, Methodology, Conceptualization. **Philippa Liggins:** Writing – review & editing, Validation, Software, Data curation.

Declaration of competing interest

The authors declare that they have no known competing financial interests or personal relationships that could have appeared to influence the work reported in this paper.

Data availability

The data used in this study can be found in Supplementary Tables 1-9. For reproducibility, the code used for data analysis has been archived on Zenodo (https://doi.org/10.5281/zenodo.8222051).

Acknowledgements

This research was supported by the Philip Leverhulme Prize (PLP-2018-362). SY, JB and ME were supported by COMET, the NERC Centre for the Observation and Modelling of Earthquakes, Volcanoes and Tectonics, a partnership between UK Universities and the British Geological Survey. JB received funding from the European Research Council (ERC) under the European Union's Horizon 2020 research and innovation programme (MAST; grant agreement No. 101003173). PL acknowledges the support by the Embiricos Trust Scholarship from Jesus College, Cambridge. The authors thank Oliver Shorttle for the helpful discussions about an earlier version of this article.

Appendix A. Fractional crystallisation

Evolved magmas (i.e., andesite, dacite and rhyolite) are likely to be more volatile-rich than less-evolved mafic magmas (i.e., basalt) due to fractional crystallisation from primitive basaltic magmas (Marty and Zimmermann, 1999; Wallace, 2005). This is because volatile enrichment occurs during fractional crystallisation, in which magma differentiates and the crystals formed during cooling are removed from the gradually solidifying melt (Rogers, 2015).

The equation for crystallisation is given as

$$C_L/C_0 = F^{D-1} \tag{A.1}$$

Here, C_0 is the original concentration of an element or species in the melt (e.g., water concentration in basaltic melt as a mass fraction), and C_L represents the final concentration after crystallisation (e.g., water concentration in the rhyolite melt). D denotes the partition coefficient of water, which is the ratio between the concentration in crystals and the melt. F represents the 'melt fraction remaining'.

For simplicity, we assume that water is completely 'incompatible' by setting D to zero:

$$C_L = C_0/F \tag{A.2}$$

Assuming 90% crystallisation of rhyolite, F is equal to 0.1. For example, if the basalt has 1 wt% H_2O, then after 90% crystallisation the rhyolite melt will have $C_L = \frac{0.01}{0.1} = 0.1$, meaning the rhyolite will have a water content of 10 wt%.

These calculations form the basis for determining the bulk water content of rhyolitic melt. However, it is important to note that during prolonged crystallisation in a magma storage region, some exsolved fluids may be lost, which means that this method provides an upper bound estimation. For basalts with 3 wt% water, rhyolites would result with over 30 wt% water. Similarly, for basalts with 1 wt% carbon dioxide and 1500 ppm sulfur, the rhyolite would have 10 wt% carbon dioxide and 15000 ppm sulfur, respectively. Such high magmatic volatile content is unlikely to be retained by the magma, as at these weight fractions, the magmatic volatiles are more likely to escape. Therefore, for our modelling, a reasonable range of values for rhyolite would be 5-15 wt% water, 1-3 wt% carbon dioxide and 1800-4200 ppm sulfur.

Appendix B. Magma density

Magma density is the weighted sum of melt density and gas density:

$$\rho_m = \rho_M V_m + \rho_g V_g \tag{B.1}$$

The melt volume fraction V_M and gas volume fraction V_g is the volume of the melt v_M and the volume of the gas v_g per unit volume of magma that consists of melt and gas respectively:

$$\rho_m = \rho_M \frac{v_M}{v_M + v_g} + \rho_g \frac{v_g}{v_M + v_g} \tag{B.2}$$

Here we introduce gas segregation v_e into Equation (B.2):

$$\rho'_m = \rho_M \frac{v_M}{v_M + v_g + v_e} + \rho_g \frac{v_g + v_e}{v_M + v_g + v_e} \tag{B.3}$$

$$\rho'_m = \frac{\rho_M v_M + \rho_g (v_g + v_e)}{v_M + v_g + v_e} \tag{B.4}$$

where ρ'_m represents magma density with additional or reduced gas content due to gas segregation. By letting $v_e = k v_g$,

$$\rho'_m = \frac{\rho_M v_M + \rho_g (v_g + k v_g)}{v_M + v_g + k v_g} \tag{B.5}$$

$$\rho'_m = \frac{\rho_M v_M + \rho_g v_g (1 + k)}{v_M + v_g (1 + k)} \tag{B.6}$$

where $k > 0$ represents pre-eruptive gas accumulation and $-1 < k < 0$, represents pre-eruptive degassing. We divide $v_M + v_g$ at both sides of the fraction:

$$\rho'_m = \frac{\rho_M v_M + \rho_g v_g (1 + k)}{v_M + v_g (1 + k)} \div \frac{v_M + v_g}{v_M + v_g} \tag{B.7}$$

Since $V_M = \frac{v_M}{v_M + v_g}$ and $V_g = \frac{v_g}{v_M + v_g}$,

$$\rho'_m = \frac{\rho_M V_M + \rho_g V_g (1 + k)}{1 + k V_g} \tag{B.8}$$

The volume fraction of melt can also be written as $V_M = 1 - V_g$ and thus:

$$\rho'_m = \frac{\rho_M (1 - V_g) + \rho_g V_g (1 + k)}{1 + k V_g} \tag{B.9}$$

which is simplified as:

$$\rho'_m = \frac{\rho_M + V_g [\rho_g (1 + k) - \rho_M]}{1 + k V_g}. \tag{B.10}$$

Appendix C. Supplementary material

Supplementary material related to this article can be found online at https://doi.org/10.1016/j.epsl.2023.118548.

References

Amoruso, A., Crescentini, L., 2009. Shape and volume change of pressurized ellipsoidal cavities from deformation and seismic data. J. Geophys. Res. 114, B02210. https://doi.org/10.1029/2008JB005946. http://doi.wiley.com/10.1029/2008JB005946.

Anderson, K., Segall, P., 2011. Physics-based models of ground deformation and extrusion rate at effusively erupting volcanoes. J. Geophys. Res., Solid Earth 116, 1–20. https://doi.org/10.1029/2010JB007939. http://doi.wiley.com/10.1029/2010JB007939.

Asimow, P.D., 1998. Algorithmic modifications extending MELTS to calculate subsolidus phase relations. Am. Mineral. 83, 1127–1132. https://doi.org/10.2138/AM-1998-9-1022/MACHINEREADABLECITATION/RIS. https://www.degruyter.com/document/doi/10.2138/am-1998-9-1022/html.

Baker, D.R., Freda, C., Brooker, R.A., Scarlato, P., 2005. Volatile diffusion in silicate melts and its effects on melt inclusions. Ann. Geophys. 48. https://doi.org/10.4401/ag-3227. https://www.annalsofgeophysics.eu/index.php/annals/article/view/3227.

Barry, P.H., Hilton, D.R., Füri, E., Halldórsson, S.A., Grönvold, K., 2014. Carbon isotope and abundance systematics of Icelandic geothermal gases, fluids and subglacial basalts with implications for mantle plume-related CO2 fluxes. Geochim. Cosmochim. Acta 134, 74–99. https://doi.org/10.1016/J.GCA.2014.02.038.

Biggs, J., Wright, T.J., 2020. How satellite InSAR has grown from opportunistic science to routine monitoring over the last decade. https://doi.org/10.1038/s41467-020-17587-6.

Burgisser, A., Alletti, M., Scaillet, B., 2015. Simulating the behavior of volatiles belonging to the C-O-H-S system in silicate melts under magmatic conditions with the software D-compress. Comput. Geosci. 79, 1–14. https://doi.org/10.1016/j.cageo.2015.03.002.

Candela, P., 1997. A review of shallow, ore-related granites: textures, volatiles, and ore metals. J. Petrol. 38, 1619–1633. https://doi.org/10.1093/PETROJ/38.12.1619. https://academic.oup.com/petrology/article/38/12/1619/1604064.

Carn, S.A., 2016. On the detection and monitoring of effusive eruptions using satellite SO2 measurements. Geol. Soc., Spec. Publ. 426, 277–292. https://doi.org/10.1144/SP426.28.

Carn, S.A., Clarisse, L., Prata, A.J., 2016. Multi-decadal satellite measurements of global volcanic degassing. https://doi.org/10.1016/j.jvolgeores.2016.01.002.

Carrier, A., Got, J.L., Peltier, A., Ferrazzini, V., Staudacher, T., Kowalski, P., Boissier, P., 2015. A damage model for volcanic edifices: implications for edifice strength, magma pressure, and eruptive processes. J. Geophys. Res., Solid Earth 120, 567–583. https://doi.org/10.1002/2014JB011485. https://onlinelibrary.wiley.com/doi/full/10.1002/2014JB011485.

Casas, A.S., Wadsworth, F.B., Ayris, P.M., Delmelle, P., Vasseur, J., Cimarelli, C., Dingwell, D.B., 2019. SO2 scrubbing during percolation through rhyolitic volcanic domes. Geochim. Cosmochim. Acta 257, 150–162. https://doi.org/10.1016/J.GCA.2019.04.013.

Cashman, K.V., 2004. Volatile controls on magma ascent and eruption. In: Geophysical Monograph Series, vol. 150, pp. 109–124. https://agupubs.onlinelibrary.wiley.com/doi/full/10.1029/150GM10.

Cashman, K.V., Sparks, R.S.J., Blundy, J.D., 2017. Vertically extensive and unstable magmatic systems: a unified view of igneous processes. Science 355. https://doi.org/10.1126/science.aag3055.

Cassidy, M., Manga, M., Cashman, K., Bachmann, O., 2018. Controls on explosive-effusive volcanic eruption styles. Nat. Commun. 9, 2839. https://doi.org/10.1038/s41467-018-05293-3. http://www.nature.com/articles/s41467-018-05293-3.

Chaussard, E., Amelung, F., Aoki, Y., 2013. Characterization of open and closed volcanic systems in Indonesia and Mexico using InSAR time series. J. Geophys. Res., Solid Earth 118 (8), 3957–3969. https://doi.org/10.1002/jgrb.50288.

Chiodini, G., Granieri, D., Avino, R., Caliro, S., Costa, A., Werner, C., 2005. Carbon dioxide diffuse degassing and estimation of heat release from volcanic and hydrothermal systems. J. Geophys. Res., Solid Earth 110, 1–17. https://doi.org/10.1029/2004JB003542. https://onlinelibrary.wiley.com/doi/full/10.1029/2004JB003542.

Colombier, M., Vasseur, J., Houghton, B.F., Cáceres, F., Scheu, B., Kueppers, U., Thivet, S., Gurioli, L., Montanaro, C., Soldati, A., Di Muro, A., Dingwell, D.B., 2021. Degassing and gas percolation in basaltic magmas. Earth Planet. Sci. Lett. 573, 117134. https://doi.org/10.1016/J.EPSL.2021.117134. https://linkinghub.elsevier.com/retrieve/pii/S0012821X21003897.

Colombier, M., Wadsworth, F.B., Gurioli, L., Scheu, B., Kueppers, U., Di Muro, A., Dingwell, D.B., 2017. The evolution of pore connectivity in volcanic rocks. Earth Planet. Sci. Lett. 462, 99–109. https://doi.org/10.1016/J.EPSL.2017.01.011.

Colombier, M., Wadsworth, F.B., Scheu, B., Vasseur, J., Dobson, K.J., Cáceres, F., Allabar, A., Marone, F., Schlepütz, C.M., Dingwell, D.B., 2020. In situ observation of the percolation threshold in multiphase magma analogues. Bull. Volcanol. 82, 1–15. https://doi.org/10.1007/s00445-020-1370-1.

Ding, S., Plank, T., Wallace, P.J., Rasmussen, D.J., 2023. Sulfur_X: a model of sulfur degassing during magma ascent. Geochem. Geophys. Geosyst. 24, e2022GC010552. https://doi.org/10.1029/2022GC010552. https://onlinelibrary.wiley.com/doi/full/10.1029/2022GC010552.

Donovan, A., Blundy, J., Oppenheimer, C., Buisman, I., 2018. The 2011 eruption of Nabro volcano, Eritrea: perspectives on magmatic processes from melt inclusions. Contrib. Mineral. Petrol. 173, 1–23. https://doi.org/10.1007/S00410-017-1425-2/TABLES/2. https://link.springer.com/article/10.1007/s00410-017-1425-2.

Ebmeier, S.K., Andrews, B.J., Araya, M.C., Arnold, D.W.D., Biggs, J., Cooper, C., Cottrell, E., Furtney, M., Hickey, J., Jay, J., Lloyd, R., Parker, A.L., Pritchard, M.E., Robertson, E., Venzke, E., Williamson, J.L., 2018. Synthesis of global satellite observations of magmatic and volcanic deformation: implications for volcano monitoring & the lateral extent of magmatic domains. J. Appl. Volcanol. 7, 1–26. https://doi.org/10.1186/s13617-018-0071-3. https://appliedvolc.springeropen.com/articles/10.1186/s13617-018-0071-3.

Edmonds, M., Woods, A.W., 2018. Exsolved volatiles in magma reservoirs. J. Volcanol. Geotherm. Res. 368, 13–30. https://doi.org/10.1016/j.jvolgeores.2018.10.018.

Eguchi, J., Dasgupta, R., 2018. A CO2 solubility model for silicate melts from fluid saturation to graphite or diamond saturation. Chem. Geol. 487, 23–38. https://doi.org/10.1016/J.CHEMGEO.2018.04.012.

Furtney, M.A., Pritchard, M.E., Biggs, J., Carn, S.A., Ebmeier, S.K., Jay, J.A., McCormick Kilbride, B.T., Reath, K.A., 2018. Synthesizing multi-sensor, multi-satellite, multi-decadal datasets for global volcano monitoring. J. Volcanol. Geotherm. Res. 365, 38–56. https://doi.org/10.1016/j.jvolgeores.2018.10.002.

Galetto, F., Pritchard, M.E., Hornby, A.J., Gazel, E., Mahowald, N.M., 2023. Spatial and temporal quantification of subaerial volcanism from 1980 to 2019: solid products, masses, and average eruptive rates. Rev. Geophys. 61, e2022RG000783. https://onlinelibrary.wiley.com/doi/full/10.1029/2022RG000783.

Ge, C., Wang, J., Carn, S., Yang, K., Ginoux, P., Krotkov, N., 2016. Satellite-based global volcanic SO2 emissions and sulfate direct radiative forcing during 2005-2012. J. Geophys. Res. 121, 3446–3464. https://doi.org/10.1002/2015JD023134. https://agupubs.onlinelibrary.wiley.com/doi/full/10.1002/2015JD023134.

Ghiorso, M.S., Sack, R.O., 1995. Chemical mass transfer in magmatic processes IV. A revised and internally consistent thermodynamic model for the interpolation and extrapolation of liquid-solid equilibria in magmatic systems at elevated temperatures and pressures. Contrib. Mineral. Petrol. 119, 197–212. https://doi.org/10.1007/BF00307281.

Global Volcanism Program, 2013. https://volcano.si.edu/. https://doi.org/10.5479/si.GVP.VOTW4-2013.

Gonnermann, H.M., Manga, M., 2006. The fluid mechanics inside a volcano. Annu. Rev. Fluid Mech. 39, 321–356. https://doi.org/10.1146/annurev.fluid.39.050905.110207. https://www.annualreviews.org/doi/abs/10.1146/annurev.fluid.39.050905.110207.

Heap, M.J., Villeneuve, M., Albino, F., Farquharson, J.I., Brothelande, E., Amelung, F., Got, J.L., Baud, P., 2020. Towards more realistic values of elastic moduli for volcano modelling. J. Volcanol. Geotherm. Res. 390, 106684. https://doi.org/10.1016/j.jvolgeores.2019.106684.

Hotta, K., Iguchi, M., Ohkura, T., Hendrasto, M., Gunawan, H., Rosadi, U., Kriswati, E., 2019. Magma intrusion and effusion at Sinabung volcano, Indonesia, from 2013 to 2016, as revealed by continuous GPS observation. J. Volcanol. Geotherm. Res. 382, 173–183. https://doi.org/10.1016/J.JVOLGEORES.2017.12.015.

Hreinsdóttir, S., Sigmundsson, F., Roberts, M.J., Björnsson, H., Grapenthin, R., Arason, P., Árnadóttir, T., Hólmjárn, J., Geirsson, H., Bennett, R.A., Gudmundsson, M.T., Oddsson, B., Ófeigsson, B.G., Villemin, T., Jónsson, T., Sturkell, E., Höskuldsson, A., Larsen, G., Thordarson, T., Óladóttir, B.A., 2014. Volcanic plume height correlated with magma-pressure change at Grímsvötn Volcano, Iceland. Nat. Geosci. 7, 214–218. https://doi.org/10.1038/ngeo2044. www.nature.com/naturegeoscience.

Jaupart, C., Allègre, C.J., 1991. Gas content, eruption rate and instabilities of eruption regime in silicic volcanoes. Earth Planet. Sci. Lett. 102, 413–429. https://doi.org/10.1016/0012-821X(91)90032-D.

Johnson, M.C., Anderson, A.T., Rutherford, M.J., 1994. Pre-eruptive volatile contents of magmas. Rev. Mineral. Geochem. 30, 281–330.

Joseph, E.P., Camejo-Harry, M., Christopher, T., Contreras-Arratia, R., Edwards, S., Graham, O., Johnson, M., Juman, A., Latchman, J.L., Lynch, L., Miller, V.L., Papadopoulos, I., Pascal, K., Robertson, R., Ryan, G.A., Stinton, A., Grandin, R., Hamling, I., Jo, M.J., Barclay, J., Cole, P., Davies, B.V., Sparks, R.S., 2022. Responding to eruptive transitions during the 2020–2021 eruption of La Soufrière volcano, St. Vincent. Nat. Commun. 13 (1), 1–15. https://doi.org/10.1038/s41467-022-31901-4. https://www.nature.com/articles/s41467-022-31901-4.

Kilbride, B.M.C., Edmonds, M., Biggs, J., 2016. Observing eruptions of gas-rich compressible magmas from space. Nat. Commun. 7, 1–8. https://doi.org/10.1038/ncomms13744. www.nature.com/naturecommunications.

Kushnir, A.R., Martel, C., Champallier, R., Arbaret, L., 2017. In situ confirmation of permeability development in shearing bubble-bearing melts and implications for volcanic outgassing. Earth Planet. Sci. Lett. 458, 315–326. https://doi.org/10.1016/j.epsl.2016.10.053.

Liggins, P., Jordan, S., Rimmer, P.B., Shorttle, O., 2022. Growth and evolution of secondary volcanic atmospheres: I. Identifying the geological character of hot rocky planets. J. Geophys. Res., Planets 127, e2021JE007123. https://doi.org/10.1029/2021JE007123. https://onlinelibrary.wiley.com/doi/full/10.1029/2021JE007123. https://onlinelibrary.wiley.com/doi/abs/10.1029/2021JE007123. https://agupubs.onlinelibrary.wiley.com/doi/10.1029/2021JE007123.

Liggins, P., Shorttle, O., Rimmer, P.B., 2020. Can volcanism build hydrogen-rich early atmospheres? Earth Planet. Sci. Lett. 550, 116546. https://doi.org/10.1016/J.EPSL.2020.116546.

Marty, B., Zimmermann, L., 1999. Volatiles (He, C, N, Ar) in mid-ocean ridge basalts: assesment of shallow-level fractionation and characterization of source composition. Geochim. Cosmochim. Acta 63, 3619–3633. https://doi.org/10.1016/S0016-7037(99)00169-6.

McKee, K., Smith, C.M., Reath, K., Snee, E., Maher, S., Matoza, R.S., Carn, S., Mastin, L., Anderson, K., Damby, D., Roman, D.C., Degterev, A., Rybin, A., Chibisova, M., Assink, J.D., de Negri Leiva, R., Perttu, A., 2021. Evaluating the state-of-the-art in remote volcanic eruption characterization Part I: Raikoke volcano, Kuril Islands. J. Volcanol. Geotherm. Res. 419, 107354. https://doi.org/10.1016/J.JVOLGEORES.2021.107354.

Nash, W.M., Smythe, D.J., Wood, B.J., 2019. Compositional and temperature effects on sulfur speciation and solubility in silicate melts. Earth Planet. Sci. Lett. 507, 187–198. https://doi.org/10.1016/J.EPSL.2018.12.006.

Newhall, C.G., 2007. Volcanology 101 for seismologists. In: Schubert, G., Kanamori, H. (Eds.), Treatise on Geophysics. Elsevier, Amsterdam, Ther Netherlands, pp. 351–388.

O'Neill, H.S., 2021. The thermodynamic controls on sulfide saturation in silicate melts with application to ocean floor basalts. In: Magma Redox Geochemistry, pp. 177–213. https://onlinelibrary.wiley.com/doi/full/10.1002/9781119473206.ch10. https://agupubs.onlinelibrary.wiley.com/doi/10.1002/9781119473206.ch10.

O'Neill, H.S.C., Mavrogenes, J.A., 2022. The sulfate capacities of silicate melts. Geochim. Cosmochim. Acta 334, 368–382. https://doi.org/10.1016/J.GCA.2022.06.020.

Oppenheimer, J., Rust, A.C., Cashman, K.V., Sandnes, B., 2015. Gas migration regimes and outgassing in particle-rich suspensions. Front. Phys., 60. https://doi.org/10.3389/FPHY.2015.00060.

Parmigiani, A., Faroughi, S., Huber, C., Bachmann, O., Su, Y., 2016. Bubble accumulation and its role in the evolution of magma reservoirs in the upper crust. Nature 532, 492–495. https://doi.org/10.1038/nature17401. http://www.nature.com/doifinder/10.1038/nature17401.

Paulatto, M., Hooft, E.E., Chrapkiewicz, K., Heath, B., Toomey, D.R., Morgan, J.V., 2022. Advances in seismic imaging of magma and crystal mush. Front. Earth Sci. 10, 970131. https://doi.org/10.3389/FEART.2022.970131/BIBTEX.

Pritchard, M.E., Poland, M., Reath, K., Andrews, B., Bagnardi, M., Biggs, J., Carn, S., Coppola, D., Ebmeier, S., Furtney, M., Girona, T., Griswold, J., Lopez, T., Lundgren, P., Ogburn, S., Pavolonis, M., Rumpf, E., Vaughan, G., Wauthier, C., Wessels, R., Wright, R., Anderson, K., Bato, M., Roman, A., 2022. Optimizing satellite resources for the global assessment and mitigation of volcanic hazards—Suggestions from the USGS Powell Center Volcano Remote Sensing Working Group. U.S. Geological Survey Scientific Investigations Report 5116. https://doi.org/10.3133/SIR20225116.

Reath, K., Pritchard, M., Biggs, J., Andrews, B., Ebmeier, S.K., Bagnardi, M., Girona, T., Lundgren, P., Lopez, T., Poland, M., 2020. Using conceptual models to relate multiparameter satellite data to subsurface volcanic processes in Latin America. Geochem. Geophys. Geosyst. 21, 1–26. https://doi.org/10.1029/2019GC008494.

Reath, K., Pritchard, M., Poland, M., Delgado, F., Carn, S., Coppola, D., Andrews, B., Ebmeier, S.K., Rumpf, E., Henderson, S., Baker, S., Lundgren, P., Wright, R., Biggs, J., Lopez, T., Wauthier, C., Moruzzi, S., Alcott, A., Wessels, R., Griswold, J., Ogburn, S., Loughlin, S., Meyer, F., Vaughan, G., Bagnardi, M., 2019. Thermal, deformation, and degassing remote sensing time series (CE 2000–2017) at the 47 most active volcanoes in Latin America: implications for volcanic systems. J. Geophys. Res., Solid Earth 124, 195–218. https://doi.org/10.1029/2018JB016199. https://onlinelibrary.wiley.com/doi/abs/10.1029/2018JB016199.

Rivalta, E., Segall, P., 2008. Magma compressibility and the missing source for some dike intrusions. Geophys. Res. Lett. 35, 1–5. https://doi.org/10.1029/2007GL032521.

Rogers, N., 2015. The composition and origin of magmas. In: The Encyclopedia of Volcanoes, pp. 93–112.

Romero, J.E., Morgavi, D., Arzilli, F., Daga, R., Caselli, A., Reckziegel, F., Viramonte, J., Díaz-Alvarado, J., Polacci, M., Burton, M., Perugini, D., 2016. Eruption dynamics of the 22–23 April 2015 Calbuco Volcano (Southern Chile): analyses of tephra fall deposits. J. Volcanol. Geotherm. Res. 317, 15–29. https://doi.org/10.1016/J.JVOLGEORES.2016.02.027.

Ruscitto, D.M., Wallace, P.J., Cooper, L.B., Plank, T., 2012. Global variations in H2O/Ce: 2. Relationships to arc magma geochemistry and volatile fluxes. Geochem. Geophys. Geosyst. 13. https://doi.org/10.1029/2011GC003887. https://agupubs.onlinelibrary.wiley.com/doi/full/10.1029/2011GC003887.

Scaillet, B., Pichavant, M., 2003. Experimental constraints on volatile abundances in arc magmas and their implications for degassing processes. Geol. Soc., Spec. Publ. 213, 23–52. https://doi.org/10.1144/GSL.SP.2003.213.01.03. http://sp.lyellcollection.org/.

Sheldrake, T.E., Aspinall, W.P., Odbert, H.M., Wadge, G., Sparks, R.S., 2017. Understanding causality and uncertainty in volcanic observations: an example of forecasting eruptive activity on Soufrière Hills Volcano, Montserrat. J. Volcanol. Geotherm. Res. 341, 287–300. https://doi.org/10.1016/J.JVOLGEORES.2017.06.007.

Sigmarsson, O., Haddadi, B., Carn, S., Moune, S., Gudnason, J., Yang, K., Clarisse, L., 2013. The sulfur budget of the 2011 Grímsvötn eruption, Iceland. Geophys. Res. Lett. 40, 6095–6100. https://doi.org/10.1002/2013GL057760. http://doi.wiley.com/10.1002/2013GL057760.

Sigmundsson, F., Hreinsdóttir, S., Hooper, A., Árnadóttir, T., Pedersen, R., Roberts, M.J., Óskarsson, N., Auriac, A., Decriem, J., Einarsson, P., Geirsson, H., Hensch, M., Ófeigsson, B.G., Sturkell, E., Sveinbjörnsson, H., Feigl, K.L., 2010. Intrusion triggering of the 2010 Eyjafjallajökull explosive eruption. Nature 468, 426–432. https://doi.org/10.1038/nature09558.

Stevenson, D.S., Blake, S., 1998. Modelling the dynamics and thermodynamics of volcanic degassing. Bull. Volcanol. 60, 307–317. https://doi.org/10.1007/s004450050234. https://link.springer.com/article/10.1007/s004450050234.

Symonds, R.B., Gerlach, T.M., Reed, M.H., 2001. Magmatic gas scrubbing: implications for volcano monitoring. J. Volcanol. Geotherm. Res. 108, 303–341. https://doi.org/10.1016/S0377-0273(00)00292-4.

Wallace, P.J., 2001. Volcanic SO2 emissions and the abundance and distribution of exsolved gas in magma bodies. J. Volcanol. Geotherm. Res. 108, 85–106. https://doi.org/10.1016/S0377-0273(00)00279-1.

Wallace, P.J., 2005. Volatiles in subduction zone magmas: concentrations and fluxes based on melt inclusion and volcanic gas data. J. Volcanol. Geotherm. Res. 140, 217–240. https://doi.org/10.1016/j.jvolgeores.2004.07.023.

Wallace, P.J., Anderson, A., Davis, A.M., 1995. Quantification of pre-eruptive exsolved gas contents in silicic magmas. Nature 377, 612–616. https://doi.org/10.1038/377612a0. https://www.nature.com/articles/377612a0.

Wallace, P.J., Gerlach, T.M., 1994. Magmatic vapor source for sulfur dioxide released during volcanic eruptions: evidence from Mount Pinatubo. Science 265, 497–499. https://doi.org/10.1126/science.265.5171.497. http://science.sciencemag.org/.

Witham, F., Blundy, J., Kohn, S.C., Lesne, P., Dixon, J., Churakov, S.V., Botcharnikov, R., 2012. SolEx: a model for mixed COHSCl-volatile solubilities and exsolved gas compositions in basalt. Comput. Geosci. 45, 87–97. https://doi.org/10.1016/j.cageo.2011.09.021.

Woods, A.W., Huppert, H.E., 2003. On magma chamber evolution during slow effusive eruptions. J. Geophys. Res. 108, 1–16. https://doi.org/10.1029/2002jb002019.

Yip, S.T.H., Biggs, J., Edmonds, M., Liggins, P., Shorttle, O., 2022. Contrasting volcanic deformation in Arc and Ocean Island settings due to exsolution of magmatic water. Geochem. Geophys. Geosyst. 23, e2022GC010387. https://doi.org/10.1029/2022GC010387. https://onlinelibrary.wiley.com/doi/full/10.1029/2022GC010387. https://onlinelibrary.wiley.com/doi/abs/10.1029/2022GC010387. https://agupubs.onlinelibrary.wiley.com/doi/10.1029/2022GC010387.